A coupled meshless element free Galerkin and radial basis functions method for Level set based topology optimization

A coupled meshless element free Galerkin and radial basis functions method for Level set based topology optimization

Baseer Ullah[a,*], Wajid Khan[a,c], Siraj-ul-Islam[a], Zahur Ullah[b]

[a] *Department of Basic Sciences, Faculty of Architecture, Allied Sciences and Humanities, University of Engineering and Technology, Peshawar, Pakistan.*
[b] *Advanced Composites Research Group, School of Mechanical and Aerospace Engineering, Queen's University, Belfast, Ashby Building, Belfast, BT9 5AH, UK.*
[c] *Higher Education, Archives and Libraries Department Government of Khyber Pakhtunkhwa, Pakistan.*

Abstract

This paper presents a meshless element free Galerkin method coupled with the radial basis functions (RBFs) based level set algorithm for topology optimization. The meshless approach provides the structural response and corresponding sensitivities at nodal/grid points, and the solution of RBFs based level set formulation updates the structural geometry accordingly. Thus, this unique and novel approach allows solution of the optimization problems using a single discretization scheme for both the meshless as well as the level set methods. A special technique is proposed for the identification of meshless nodal points within the solid and void regions of the structural geometry. The present method handles the appropriate topological modifications, i.e., hole creation, splitting, merging, etc., affectively. Optimal solutions of the benchmark problems suggest reliability and compatibility of the proposed approach versus the mesh based techniques available within the structural optimization literature.

Keywords: Topology optimization, Radial basis functions, Element free Galerkin method, Minimum compliance, Level set method.

1. Introduction

Structural optimization is an active field of research. A number of methods are reported in the literature, for size, shape and topology optimization (TO). Besides the size and shape optimization techniques, TO has gained much attention from the researchers, due to its importance and versatility [1, 4, 5]. The available procedures optimize the given objective function under different constraints, e.g., the minimum compliance with optimal distribution of the given material within the design domain,

*Corresponding author
Email address: baseerullah@gmail.com (Baseer Ullah)

[6,7]. Numerous numerical procedures including: homogenization method [8–10], solid isotropic material with penalization (SIMP) method [11], evolutionary structural optimization (ESO) [12], bi-directional ESO [13], and level set based optimization methods [14–17] have been reported, with each one have its own merits and de-merits. The TO based procedures have high end applications in various design and engineering processes as described in details in [18].

The homogenization and SIMP based TO approaches are basically density based, where the geometry is stated through a material distribution of two or more phases. The material is typically element wise or nodal shape functions in these approaches. The element wise density may cause instabilities like local minima, mesh-dependency, and checkerboard pattern [19]. Similar deficiencies are also associated with the progressive removal/addition of material in the ESO/BESO approaches [20].

The other major class of TO techniques are based on the implicit representation of the structural geometry using the level set function [14,15,21,22]. The front tracking level set formulation was mainly designed for the interface problems, but later on it found relevance in image processing, computer animations, optics, fluid mechanics and related interface problems [14,15,23–28]. The level set method (LSM) was first used in the field of structural optimization in [23]. As the conventional LSM based optimization methods cannot nucleate holes during the optimization process, especially in two-dimensions, and mostly the optimal solutions are dependent on the initially guessed topology. For automatic hole nucleation, a combination of shape and topological derivatives within the LSM based optimization method has been implemented in [29]. The LSM was further utilised using the fictitious interface energy for both two and three-dimensional optimization problems in [30]. Implementation of the topological derivatives for automatic hole nucleation during the optimization process have been found inconvenient [31–33]. Whereas, the RBFs based LSM coupled with the Erastz material approach [31, 34], allows automatic hole nucleation for two-dimensional geometry.

Research interests in the RBFs applications for the numerical solution of PDEs have been amplified manifolds. Specifically, related to our work, the meshless formulation based RBFs have been put forward for the Hamilton Jacobi PDE in [35]. The LSM using local and global RBFs have been reported in [31,34,36]. Compared to the conventional LSM of directly solving the HJ equation [37,38], the RBFs based LSM (RBFs-LSM) track the evolving geometry of the structure by updating the RBFs coefficients at nodal points. The RBFs-LSM has been used for active contour and active surface modelling [39], symmetry and pattern repetition constraints [40]. Due to the use of MQ RBFs with global support, a relatively smooth level set evolution can be maintained without reinitialization [41].

There are a variety of PDE models which are arising from the real world applications with the context of meshless methods (MM) are discussed in details in [42, 43]. The main benefit of MM is their implementation simplicity, which is based on nodes (regardless of their connectivity information) rather than the mesh (which is a pre-processing requirement in the mesh-based methods). The other useful property of the MM is the virtual conversion of a higher dimensional space problem into a lower dimension [44]. Moreover, the simplicity of implementation, high accuracy and rapid convergence makes the MM very attractive for researchers [45]. The first MM namely, the smooth particle hydrodynamic (SPH) was introduced in 1977 [46]. The global weak form MM introduced in 1994 was the Element Free Galerkin Method (EFGM) [47]. The EFG method generally provide a very good numerical stability and accuracy for computational mechanics problems. The other popular meshless approaches are: Point Interpolation Method [48], Reproducing Kernel Particle Method (RKPM) [49], partition of unity method [50], meshless Petrov Galerkin method [51].

Most of the topology optimization approaches use the finite element method (FEM) as a structural analysis tool, however, it still suffers from high processing time, low accuracy of stresses, difficulty in incorporating adaptivity as well as handling large deformation, moving boundaries, etc., problems. There exist many other techniques for the numerical solution of topology optimization problems, however, the MM is an ideal choice as it provides a reliable solution without compromising the required accuracy as well as numerical stability for certain class of problems; only using a set of nodes without any mesh connectivity information. In this regard an initial implementation of the meshless EFG formulation equipped with the conventional LSM was proposed in [52]. The hole nucleation was accomplished with the implementation of topological derivatives in the form of a source term in the Hamilton Jacobi (HJ) type equation. However, to completely eliminate the dependency of initially guessed topology and the use of topological derivatives, a novel approach is presented in this work, where the level set function is parametrized with the RBFs and is integrated with the EFG approach for the solution of topology optimization problems. An important aspect of this new implementation is the modelling of the moving boundary discontinuities without re-discretization. Moreover, the same computational grid is used for both the meshless EFG and RBFs-LSM, which allows significant saving of the overall computational efforts.

In topology optimization literature, the mesh based numerical methods are extensively used, which are mainly based on an explicit mesh for discretization and numerical approximation purposes. The nature of large deformation and moving boundaries problems demand frequent re-meshing for numerical

solution which are unavoidable. Furthermore, the nonlinear behaviour of large deformation poses complication and difficulties in handling some challenging problems, e.g., topology optimization of vehicle crashworthiness analysis etc., which limits the use of the mesh based methods for these problems. However, the emergence and advancement of the meshless methods in the field of topology optimization can be considered as an effective tool for the numerical solution of some of the challenging problems, such as large deformation and moving boundaries. Generally, the meshless weak form methods are computationally expensive than the mesh based methods. However, the meshless methods have high order of convergence as well as smooth strains and stresses than the mesh based methods.

The methodology proposed in this research work is as follows. The unknown solution in the linear elasticity equation is approximated with the moving least square (MLS) shape functions and the Galerkin technique of global weak form is employed to discretize the state equation. The Dirichlit boundary conditions are incorporated with the help of Lagrange multiplier technique. The implicit geometric representation is done with the multi-quadric RBF. The propagation of the structural geometry is updated through a numerical solution of coupled ODEs, the semi-discretized form of the HJ type PDE. In the optimization process, an approximate re-initialization technique is used to circumvent high peaks of the gradient and to facilitate hole creation in a stable fashion. The proposed method is applied for the minimum compliance of two-dimensional structural optimization problem. Several benchmark tests are chosen from the literature to ascertain relatively simple applicability of the proposed method.

In this implementation, only for numerical integration and approximation, background cells are utilized without the need of any mesh. This suggests that this new implementation can effectively handle large deformation problems without any mesh distortion issues, and this would be seen as a potential of the use of this method for topology optimization of nonlinear structures undergoing large deformation. Furthermore, this aspect of the proposed approach is definitely of a great importance for future topology optimization research of many important and critical mechanical components in aerospace as well as auto-mobiles industries.

The rest of the paper is summarized as follows. In Section 2 the EFG method and MLS shape functions are discussed briefly. The RBFs based LSM is presented in Section 3. The EFG method coupled with RBFs based LSM is discussed in section 4. The minimum compliance model is discussed in Section 5. The numerical examples are discussed in Section 6 and conclusions are drawn in Section 7, respectively.

2. EFG formulation for the equilibrium equation

In this section, the EFG method based variational form is discussed for completeness. Let $\Omega \subset R^d$ (for $d = 2$ or 3) be a domain with boundary $\Gamma = \Gamma_u \cup \Gamma_t$, where Γ_t, Γ_u represents the Neumann and Dirichlet boundaries, respectively. The following two-dimensional linear elasticity model along with the boundary information is considered:

$$\sigma_{ij,j}(\mathbf{x}) + b_i(\mathbf{x}) = 0; \quad \text{for} \quad \mathbf{x} \in \Omega, \tag{1}$$

with boundary conditions:

$$u_i = \bar{u} \quad \text{on} \quad \mathbf{x} \in \Gamma_u, \tag{2}$$

and

$$t_i = \bar{t} \quad \text{on} \quad \mathbf{x} \in \Gamma_t. \tag{3}$$

The symbol σ represents the Cauchy stress tensor, $\boldsymbol{u} = (\boldsymbol{u}_1, \ldots, \boldsymbol{u}_n) = (u_1, v_1, \ldots, u_n, v_n)^T$ is the displacement vector, and b is the body force. The traction component is given by

$$t_i = \sigma_{ij}(\mathbf{x})\boldsymbol{n_i}, \quad \mathbf{x} \in \Gamma, \tag{4}$$

where $\boldsymbol{n_i}$ is the normal vector.

The weak formulation of Eq. (1) is given as

$$\int_\Omega v_i[\sigma_{ij,j}(\mathbf{x}) + b_i(\mathbf{x})]d\Omega = 0, \tag{5}$$

where v_i is the weight function. In most of the meshless methods, the moving least square shape functions are used to approximate the unknown solutions. The Dirichlet boundary condition implementation in the EFG is comparatively problematic due to non-compliance of Kronecker delta property. Several techniques such as Lagrange multiplier, Nitsche's, penalty and coupling with finite elements are available in the literature with their associated merits and demerits to handle this issue, as mentioned in [2,3,53,54]. However, in the current implementation, the commonly used method of Lagrange multipliers technique is used to incorporate the Dirichlit boundary condition in the weak form. After this, the weak form Eq. (5) becomes

$$\int_\Omega \delta(D\boldsymbol{u})^T C(D\boldsymbol{u})d\Omega - \int_\Omega \delta\boldsymbol{u}^T b d\Omega - \int_{\Gamma_t} \delta\boldsymbol{u}^T \bar{t} d\Gamma - \int_{\Gamma_u} \delta\eta^T(\boldsymbol{u} - \bar{u})d\Gamma - \int_{\Gamma_u} \delta\boldsymbol{u}^T \eta d\Gamma = 0, \tag{6}$$

where the quantities $\delta\eta$ and $\delta\boldsymbol{u}$ present variations of the Lagrange multiplier η and displacement $\boldsymbol{u}$. In Eq. (6) the differential operator matrix D is given as

$$D = \begin{bmatrix} \frac{\partial}{\partial x} & 0 & 0 \\ 0 & \frac{\partial}{\partial y} & 0 \\ \frac{\partial}{\partial y} & \frac{\partial}{\partial x} & 0 \end{bmatrix}. \tag{7}$$

After simplification, the system of equations stemming from the above equation can be written as

$$\begin{pmatrix} K & G \\ G^T & 0 \end{pmatrix} \begin{pmatrix} \boldsymbol{u} \\ \eta \end{pmatrix} = \begin{pmatrix} f \\ q \end{pmatrix}. \tag{8}$$

The global stiffness matrix K and force vector f are given as

$$K_{IJ} = \int_{\Omega} B_I^T C B_J d\Omega, \tag{9}$$

$$f_I = \int_{\Omega} \phi_I b d\Omega + \int_{\Gamma_t} \phi_I \bar{t} d\Gamma, \quad I, J = 1, 2, \ldots, N. \tag{10}$$

The matrices B and C are

$$B = \begin{pmatrix} \phi_{I,x} & 0 \\ 0 & \phi_{I,y} \\ \phi_{I,x} & \phi_{I,y} \end{pmatrix}, \tag{11}$$

and for plane stress case

$$C = \frac{E}{1-\upsilon^2} \begin{pmatrix} 1 & \upsilon & 0 \\ \upsilon & 1 & 0 \\ 0 & 0 & \frac{1-\upsilon}{2} \end{pmatrix}, \tag{12}$$

where the elasticity parameters υ, E are the Poisson's ratio and Young's modulus respectively. The matrices G and q are

$$G_{IJ} = \int_{\Gamma_u} \phi_I M_J d\Gamma, \tag{13}$$

and

$$q_J = \int_{\Gamma_u} M_J \bar{u} d\Gamma, \tag{14}$$

where M_J denotes the Lagrange interpolating polynomials.

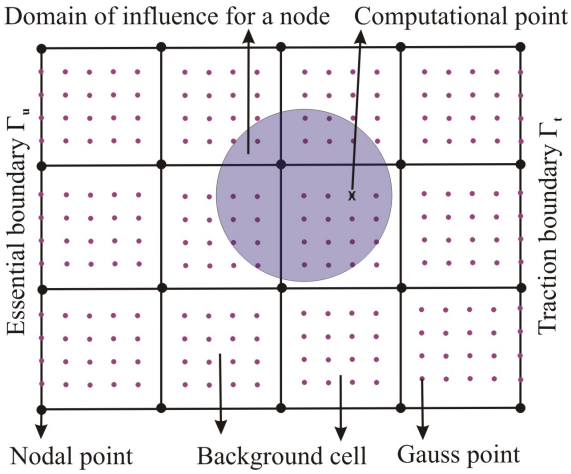

Figure 1: Graphical representation of the EFG method.

Getting the solution vector $\boldsymbol{u}$ from Eq. (8), the strain field can be obtained as:

$$
\begin{aligned}
\epsilon &= D\boldsymbol{u}^h \\
&= \begin{bmatrix} \frac{\partial}{\partial x} & 0 \\ 0 & \frac{\partial}{\partial y} \\ \frac{\partial}{\partial y} & \frac{\partial}{\partial x} \end{bmatrix} \begin{bmatrix} \phi_1 & 0 & \dots \phi_n & 0 \\ 0 & \phi_1 & \dots 0 & \phi_n \end{bmatrix} \begin{Bmatrix} u_1 \\ v_1 \\ \vdots \\ u_n \\ v_n \end{Bmatrix} \\
&= \begin{bmatrix} \phi_1, x & 0 & \dots & \phi_n, x & 0 \\ 0 & \phi_1, y & \dots & 0 & \phi_n, y \\ \phi_1, y & \phi_1, x & \dots & \phi_n, y & \phi_n, x \end{bmatrix} \begin{Bmatrix} u_1 \\ v_1 \\ \vdots \\ u_n \\ v_n \end{Bmatrix}
\end{aligned}
$$

$$
\epsilon = B\boldsymbol{u} = \sum_{j=1}^{n} B_j \boldsymbol{u}_j, \tag{15}
$$

where n is local support domain size, u_j and v_j are the j^{th} nodal point displacements and B_j is the strain matrix. In Fig. 1, visual representation of the sub-domain of influence, the background cell structure and 4×4 Gaussian quadrature points is shown. In the light of Eq. (15), representation of stress becomes

$$
\sigma = C\epsilon = CB\boldsymbol{u} = \sum_{j=1}^{n} CB_j \boldsymbol{u}_j. \tag{16}
$$

Finally, the nodal strain energy is

$$S = \frac{1}{2}\sigma^t \epsilon = \sum_{j=1}^{n} \frac{1}{2} \boldsymbol{u}_j {B_j}^t C B_j \boldsymbol{u}_j, \tag{17}$$

where ϵ and σ are the strain and cauchy stress tensor at every point.

The shape function in the EFG method is constructed with the moving least square approximation, which was proposed in [55]. In the next section, we describe the MLS method briefly.

2.1. Moving least squares shape functions

Initially, the MLS method was used in diffuse element method (DEM) [56]. Later on, the DEM was changed to EFG method [57]. The EFG approximation $\boldsymbol{u}^h(\mathbf{x})$ is defined as:

$$\boldsymbol{u}(\mathbf{x}) \approx \boldsymbol{u}^h(\mathbf{x}) = \sum_{k=1}^{l} p_k(\mathbf{x}) d_k(\mathbf{x}) = P^T(\mathbf{x}) \boldsymbol{d}(\mathbf{x}), \tag{18}$$

where $\boldsymbol{d}(\mathbf{x})$ is the unknown coefficients. The vector P is given as

$$P^T(\mathbf{x}) = [p_1(\mathbf{x}), p_2(\mathbf{x}), \ldots, p_l(\mathbf{x})]. \tag{19}$$

In order to find the unknown coefficients, consider the following functional:

$$J(\mathbf{x}) = \sum_{k=1}^{n} [(\boldsymbol{P}^T(\mathbf{x}_k)\boldsymbol{d}(\mathbf{x}) - \boldsymbol{u}_k)^2 v(||\mathbf{x} - \mathbf{x}_k||)], \tag{20}$$

where $v(\mathbf{x})$ is the cubic spline weight function defined in [53, 54]. Minimizing Eq. (20) gives:

$$N(\mathbf{x})d(\mathbf{x}) = F(\mathbf{x})u(\mathbf{x}), \tag{21}$$

where $N(\mathbf{x})$ and $F(\mathbf{x})$ are defined as follows:

$$N(\mathbf{x}) = P^T V P = \sum_{k=1}^{n} v_k(\mathbf{x}) p_k(\mathbf{x}) {p_k}^T(\mathbf{x}), \tag{22}$$

$$F(\mathbf{x}) = P^T V = [p_1(\mathbf{x})v_1(\mathbf{x}), p_2(\mathbf{x})v(\mathbf{x}), \ldots, p_n(\mathbf{x})v_n(\mathbf{x})]. \tag{23}$$

Finally, the shape function is given by

$$\phi^T(\mathbf{x}) = P^T(\mathbf{x}) N^{-1}(\mathbf{x}) F(\mathbf{x}), \tag{24}$$

or

$$\phi_r^T(\mathbf{x}) = \sum_{k=1}^{n} p_k(\mathbf{x}) (N^{-1}(\mathbf{x})F(\mathbf{x}))_{kr} = P^T(\mathbf{x}) N^{-1}(\mathbf{x}) F(\mathbf{x}), \tag{25}$$

for $r = 1, \ldots, n$.

Hence, the partial derivative of the shape function with respect to x is given by

$$\phi_{r,x} = P^T_{,x} N^{-1} F_r + P^T[(N^{-1})_{,x} F_r + N^{-1} F_{r,x}]. \tag{26}$$

In the next section, the structural geometry representation will be described within the RBFs and LSM frame work.

3. Radial basis functions within the LSM context

The conventional level set method [14, 15] is employed to move the front during the optimization process. The implicit mathematical form of the interface in the form of level set function (LSF) is given as $\Gamma = \{\mathbf{x} \in \Omega \subset R^d | \Psi(\mathbf{x}) = 0\}$. Propagation of the LSF is undertaken through the following PDE [58]

$$\frac{\partial \Psi}{\partial t} + v| \bigtriangledown \Psi| = 0, \quad \Psi(\mathbf{x}, t = 0) = \Psi_0(\mathbf{x}), \tag{27}$$

where v is the speed along the normal. The PDE (27) is prone to numerical instabilities which can be skipped using upwinding and implementation of CFL condition. In some situations, the unwanted wiggly peaks are clipped by re-initialization scheme [34]. The periodic re-initialization of the LSF increases the computational cost of the optimisation technique. Also the new hole creation capability of the LSF during the optimization process is suppressed due to the re-initialization of the LSF. In order to overcome these issues of the conventional LSM, an alternative approach [34], which is based on the parametrization of the level set using the RBFs was proposed. In the next section, we shed some light on this approach.

3.1. Radial basis functions based LSM

Here we review the RBFs based LSM first introduced in [31, 34, 38]. A radially symmetric function at $\mathbf{x}_i$ is defined as [59]

$$\Psi_i(\mathbf{x}) = \psi(||\mathbf{x} - \mathbf{x}_i||), \tag{28}$$

where $||.||$ is a Euclidean norm and $\mathbf{x} = (x, y)$. The shape parameter, i.e., c, dependent radial basis function used here is defined as

$$\Psi_i(\mathbf{x}) = \sqrt{(\mathbf{x} - \mathbf{x}_i)^2 + c^2}. \tag{29}$$

The interpolation of any function Ψ through MQ RBF is

$$\Psi(\mathbf{x}) = \sum_{i=1}^{N} \alpha_i \psi_i(\mathbf{x}) + P(\mathbf{x}), \tag{30}$$

where α_i are the unknown coefficients and $P(\mathbf{x}) = \beta_0 + \beta_1 x + \beta_2 y$ is a linear polynomial. The linear polynomial is appended with the RBF to improve the conditional positive definiteness of the RBF matrix [31].

Consequently, the following system of $N + 3$ equations is formed:

$$\mathbf{H}\alpha = \mathbf{f}, \tag{31}$$

where

$$\mathbf{H} = \begin{bmatrix} A & P \\ P' & 0 \end{bmatrix},$$

$$A = \begin{bmatrix} \psi_1(\mathbf{x}_1) & \dots & \psi_N(\mathbf{x}_1) \\ \dots & \ddots & \dots \\ \psi_1(\mathbf{x}_N) & \dots & \psi_N(\mathbf{x}_N) \end{bmatrix},$$

$$P = \begin{bmatrix} 1 & x_1 & y_1 \\ \vdots & \vdots & \vdots \\ 1 & x_N & y_N \end{bmatrix},$$

,

$$\alpha = \begin{bmatrix} \alpha_1 & \dots & \alpha_N & p_0 & p_1 & p_2 \end{bmatrix}^T,$$

and

$$\mathbf{f} = \begin{bmatrix} f_1 & \dots & f_N & 0 & 0 & 0 \end{bmatrix}^T.$$

Eq. (30) becomes

$$\Psi = \psi\alpha, \tag{32}$$

where $\Psi^T = \begin{bmatrix} \psi_1 \dots \psi_N & 1 & x & y \end{bmatrix}$.

The pseudo time incorporated in the solution is represented by α as follows, we have

$$\Psi(\mathbf{x}) = \psi(\mathbf{x})^T \alpha(t). \tag{33}$$

Making use of Eq. (33) in Eq. (27), we get the following equation

$$\mathbf{H}\frac{d\alpha}{dt} + \mathbf{B}(\alpha, \mathbf{t}) = 0, \tag{34}$$

where

$$\mathbf{B}(\alpha, \mathbf{t}) = \begin{bmatrix} v(\mathbf{x_1})| \bigtriangledown \Psi(\mathbf{x}_1)^T \alpha| \\ \vdots \\ v(\mathbf{x_N})| \bigtriangledown \Psi(\mathbf{x}_N)^T \alpha| \\ 0 \\ 0 \\ 0 \end{bmatrix}.$$

Using the first-order Euler approximation, we get:

$$\alpha(t_{i+1}) = \alpha(t_i) + dt\mathbf{H}^{-1}\mathbf{B}(\alpha(t_i), t_i), \tag{35}$$

where dt is the CFL restricted time step.

As mentioned earlier, when wiggles appear in the solution, the normalization procedure of the gradient of the solution proposed in [39] is utilized in the current work as well. This procedure is put forward by setting $| \bigtriangledown \Psi| = 1$.

$$\Psi'' = \frac{\Psi}{\text{mean}(| \bigtriangledown \psi_1^0|, | \bigtriangledown \psi_2^0|, \dots | \bigtriangledown \psi_r^0|)}.$$

Since the relation between Ψ and α is linear, therefore

$$\alpha'' = \frac{\alpha}{\text{mean}(| \bigtriangledown \psi_1^0|, | \bigtriangledown \psi_2^0|, \dots | \bigtriangledown \psi_r^0|)}.$$

The function $\delta(\Psi)$ approximated as

$$\delta(\Psi) = \begin{cases} 0, & \Psi > \Delta, \\ \frac{3}{4\Delta}(1 - \frac{\Psi^2}{\Delta^2}), & -\Delta \leq \Psi \leq \Delta, \\ 0, & \Psi < -\Delta, \end{cases}$$

where Δ is the threshold value used to control the unwanted peaks in the LSF. After this intervention, the final expression for α is

$$\alpha(t_{i+1}) = \alpha''(t_i) + dt\mathbf{H}^{-1}\hat{B}(\alpha''(t_i), t_i), \tag{36}$$

where $\hat{B}$ is given by

$$\hat{B} = \begin{bmatrix} v(x_1, t_i)\delta(\Psi(x_1, \alpha''(t_i))) \\ \vdots \\ v(x_N, t_i)\delta(\Psi(x_N, \alpha''(t_i))) \\ 0 \\ 0 \\ 0 \end{bmatrix}. \tag{37}$$

Once, the structural analysis tool and structural geometry is presented, a unique coupling of the two methods will be explained in detail in the next section.

4. Coupling of EFG with RBFs based LSM

The focus of this section is on the technique designed for movement of the discontinuous boundary without re-meshing. The technique eases the amount of work required for mesh based procedure, which is utilized by both the EFG and RBFs-LSM. At every nodal point, the LSF representation is based on the convention that positive value is used for solid material and negative value for void material. So, in terms of the LSF, the point-wise nodal density function is

$$\rho(\mathbf{x}) = \begin{cases} 1 & \text{if} \quad \Psi_j >= 0, \\ 0.0001 & \text{if} \quad \Psi_j < 0. \end{cases} \tag{38}$$

For the sake of stiffness matrix invertibility, the value of ρ is taken as 0.0001 instead of zero.

$$E(\mathbf{x}) = \rho(\mathbf{x}) E_0. \tag{39}$$

Here in Eq. (39), E_0 represents the solid-state Young's modulus. Hence, the matrix C in Eq. (12) can easily be obtained using Eq. (39), after updating the level set function, which will modify the structural geometry at each optimization stage.

5. Compliance minimization problem

The proposed approach is implemented for the solution of minimum compliance problems which can also be applied to other types of objective functions too. The compliance minimization formulation for static elastic structure under volume constraint is given as

$$\text{Minimize:} \quad J(\boldsymbol{u}, \Psi) = \int_{\Omega} \epsilon(\boldsymbol{u}) : C : \epsilon(\boldsymbol{u}) H(\Psi) d\Omega,$$

subject to the constraints:

$$\begin{cases} a(\boldsymbol{u}, \delta\boldsymbol{u}, \Psi) = l(\delta\boldsymbol{u}, \Psi), \quad \forall \quad \delta\boldsymbol{u} \in H^1 \\ G(\Psi) = \int_{\Omega} H(\Psi) d\Omega - V_{req} \leq 0, \\ \boldsymbol{u} = \bar{\boldsymbol{u}}, \quad \text{on} \quad \Gamma_u \\ C : \epsilon(\boldsymbol{u}).n = \hat{t}, \quad \text{on} \quad \Gamma_t. \end{cases} \tag{40}$$

The quantities $a(\boldsymbol{u}, \delta\boldsymbol{u}, \Psi)$ and $l(\delta\boldsymbol{u}, \Psi)$ in Eq. (40) are given as

$$a(\boldsymbol{u}, \delta\boldsymbol{u}, \Psi) = \int_{\Omega} \epsilon(\boldsymbol{u}) : C : \epsilon(\boldsymbol{u}) H(\Psi) d\Omega, \tag{41}$$

and

$$l(\delta\boldsymbol{u}, \Psi) = \int_{\Gamma_t} \hat{t}\delta\boldsymbol{u} d\Gamma + \int_{\Omega} b\delta\boldsymbol{u} H(\Psi) d\Omega. \tag{42}$$

In Eq. (40), $J(\Psi)$, ϵ, $\boldsymbol{u}$, and H are the objective function, linearized strain tensor, displacement and Heaviside function, respectively. In Eq. (40), $G(\Psi)$ is the volume difference between the attained volume and the target volume V_{req} of the structure. The optimization process is carried forward in the following form [38]

$$\mathcal{L}(\boldsymbol{u}, \Psi, \lambda) = J(\boldsymbol{u}, \Psi) + \lambda G(\Psi), \tag{43}$$

where λ is a Lagrange multiplier and the constraint function is defined as

$$G(\Psi) = \int_{\Omega} H(\Psi) d\Omega - V_{req}. \tag{44}$$

According to the shape derivative in [40], the gradient decent direction is given as

$$v_N = \epsilon(\boldsymbol{u}) C \epsilon(\boldsymbol{u}) - \lambda. \tag{45}$$

Hence, the normal velocity is naturally available at all node points. In Eq. (45), λ is updated in the following manner [38]

$$\lambda^{k+1} = \begin{cases} \mu G^k & k \leq N_{it} \\ \lambda^k + \gamma^k G & k > N_{it}, \end{cases} \tag{46}$$

where γ and μ are the parameters and N_{it} represents iterations. Updated value of the parameter γ can be obtained as [38]

$$\gamma^{k+1} = \min(\gamma^k + d\gamma, \gamma_{max}), \quad k > N_{it}. \tag{47}$$

The sensitivities are smoothed to avoid very sharp changes between the neighbouring nodes as in [60]. Though, this step may not be required but better results can be obtained with excellent geometrical description of the optimal structure.

Schematic of the optimization process is shown in Fig. 2.

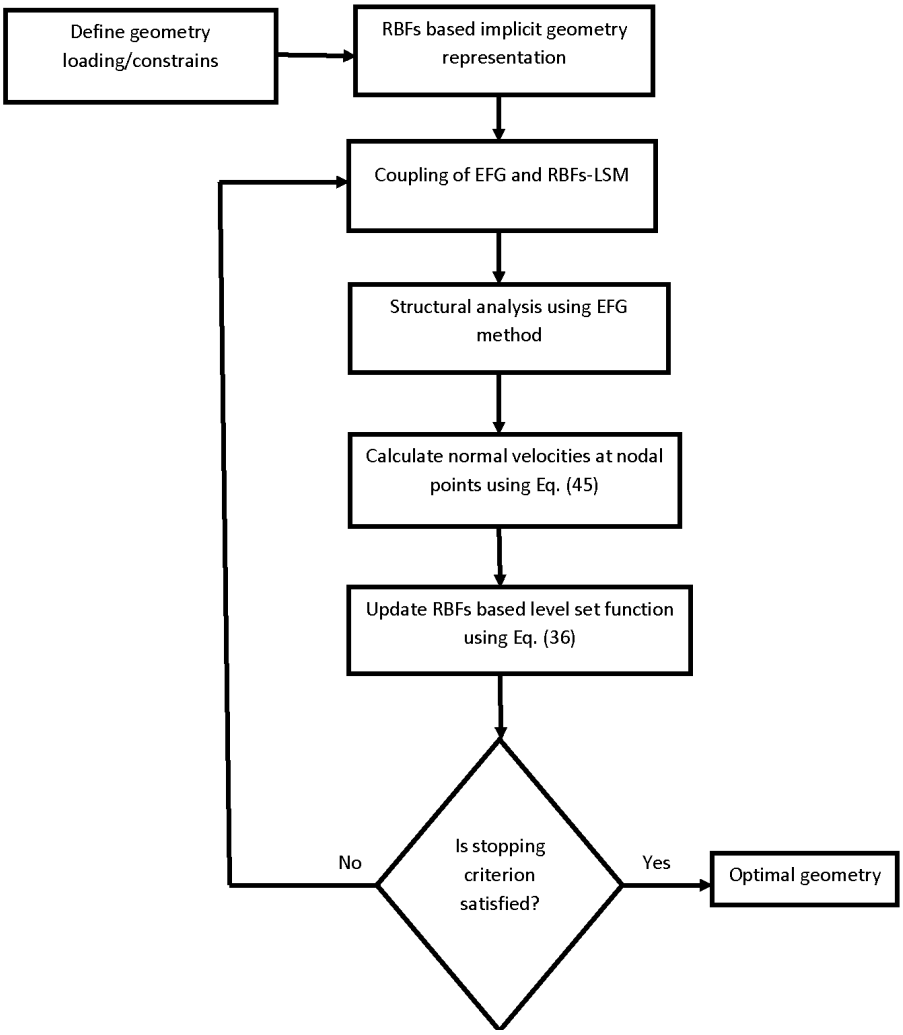

Figure 2: Schematic diagram of the optimization algorithm.

6. Implementation

To check effectiveness and reliability of the present method, four test cases with different load and boundary conditions are selected for the solution of minimum compliance objective function. For all investigated numerical problems, the shape parameter value $c = 10^{-4}$, (which is based on the numerical experiments conducted and the golden search method. Different values of c changes the shape of the approximating function. Small c leads to flat RBF, whereas large c results in high humped RBF), and the material properties are taken as: $\upsilon = 0.3$, $E = 1$ for solid and $E = 10^{-4}$ for void material. A unit point load is taken in all investigated test problems.

Four nodes per cell have been used in all problems. A 4×4 Gauss quadrature points are taken in each cell for the sake of numerical integration in global stiffness matrix given in Eq. (9). The support size is equal to two times the nodal spacing. The optimization process terminates when the relative

error of the objective function attains 10^{-5}.

6.1. Example-1

In this computational analysis we consider a cantilever beam having an aspect ratio of $1:1$. The beam left hand boundary is fixed and load is applied at the bottom right corner. The domain is discretized with $31 \times 31 = 961$ uniform nodes.

Figure 3: Design domain Example-1

The initial configuration of the structure along with boundary information are given in Fig. 3. The required volume fraction is 40% in this case. Fig. 4 shows meshless nodal points plots, where the red dots show the presence of material and black dots are devoted to void regions, respectively. Fig. 5 displays the zero level set plots of the evolving structure during the optimization process. The holes nucleation is evident around iteration 10. In the subsequent iterations hole nucleation and merging continues until the end of the optimisation process, which terminated at iteration number 87, with final geometry as depicted in Fig. 5(f). The optimal design obtained through the proposed implementation (i.e., EFG based RBFs-LSM) resembles with those reported in [61, 62]

In Fig. 6 the evolution of objective function and volume fraction is depicted. In the initial iterations material is gradually removed through hole nucleation and boundary movement, as a result compliance increases until iteration 33. Afterwards, once the volume constraint is satisfied only shape optimisation takes place which gradually adjust the available material within the design domain until the required criterion is satisfied at iteration 87.

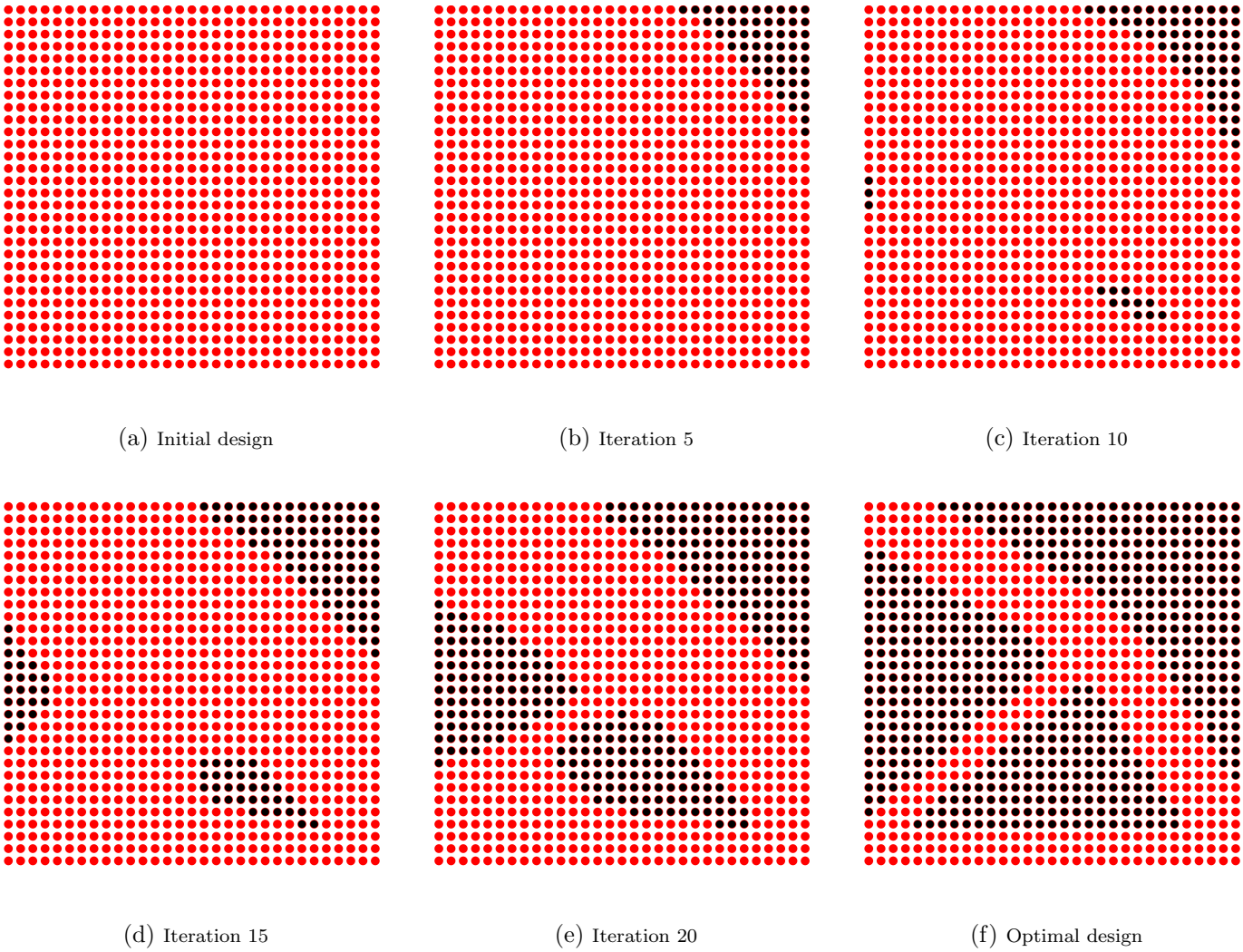

(a) Initial design (b) Iteration 5 (c) Iteration 10

(d) Iteration 15 (e) Iteration 20 (f) Optimal design

Figure 4: Meshless nodal points plots for Example-1

This problem has also been solved with the same number of nodes and volume fraction using the EFG based conventional LSM approach as reported in [52], where the topological derivative term is used in the HJ equation for hole nucleation. The optimisation process converged after 84 iterations. Numerical results comparison is shown in Fig. 7. It is evident that the RBFs-LSM method is capable of achieving the same optimal design with automatic hole nucleation capability without evaluating the topological sensitives as required in [52], which is a clear advantage of the current implementation.

Comparison of the evolution histories of both the methods is depicted in Fig. 8. The current method converged faster than the Conventional LSM (Conv-LSM) based approach though the compliance of the later is slightly less than the former.

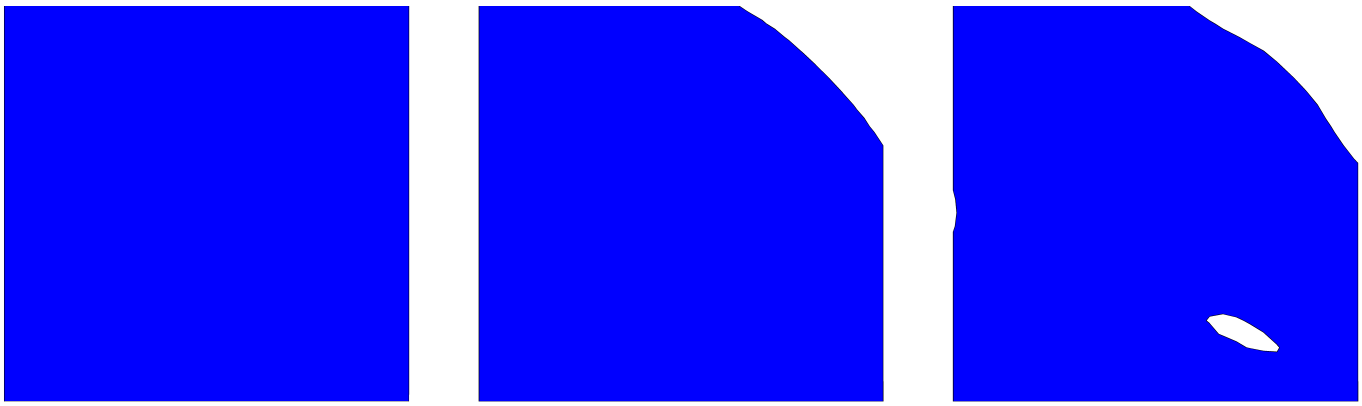

(a) Initial design (b) Iteration 5 (c) Iteration 10

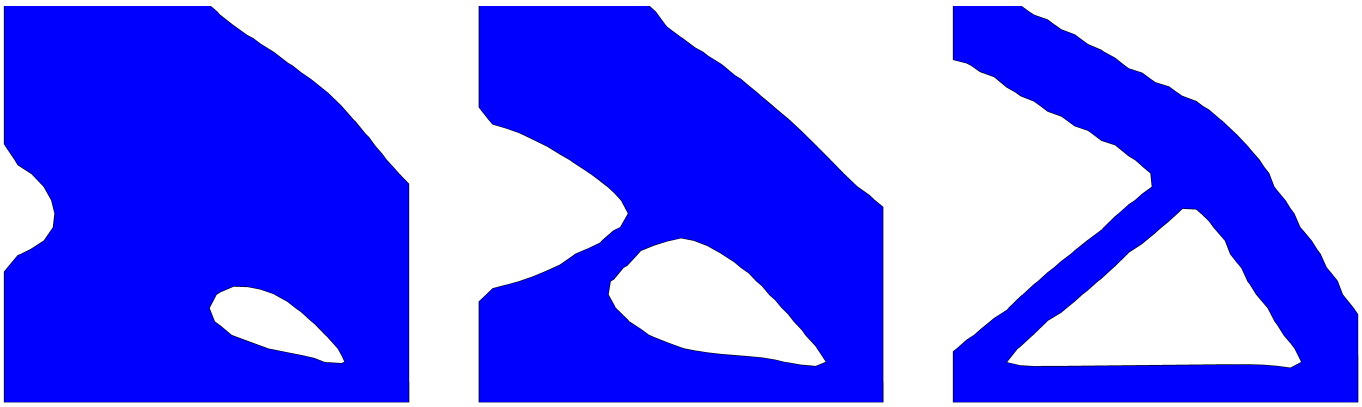

(d) Iteration 15 (e) Iteration 20 (f) Optimal design

Figure 5: Structural zero level set plots for Example-1

Finally, the optimal design contour plot is compared with the results of discrete LSM based optimization method [60] using the same initial design domain. It is evident from this comparison that the present method provides optimal design with better geometrical description.

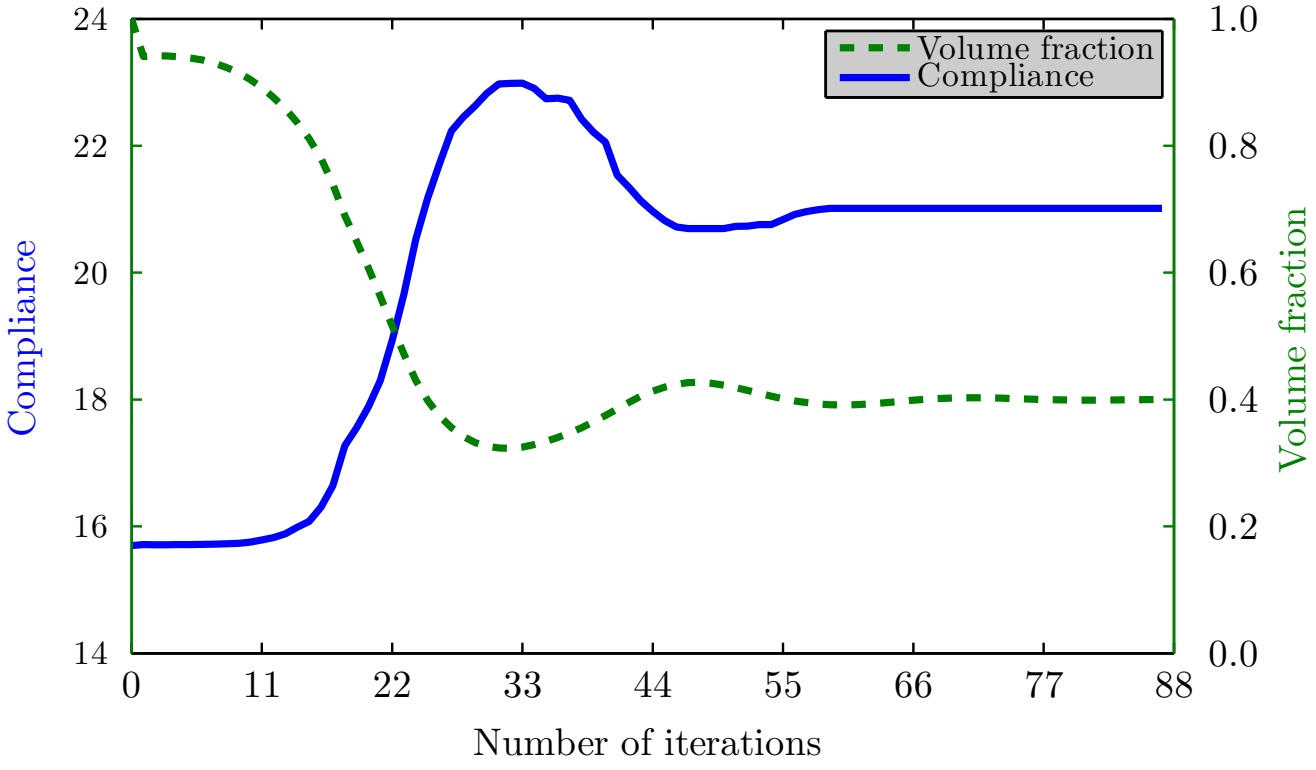

Figure 6: Objective function and volume constraint plot for Example-1

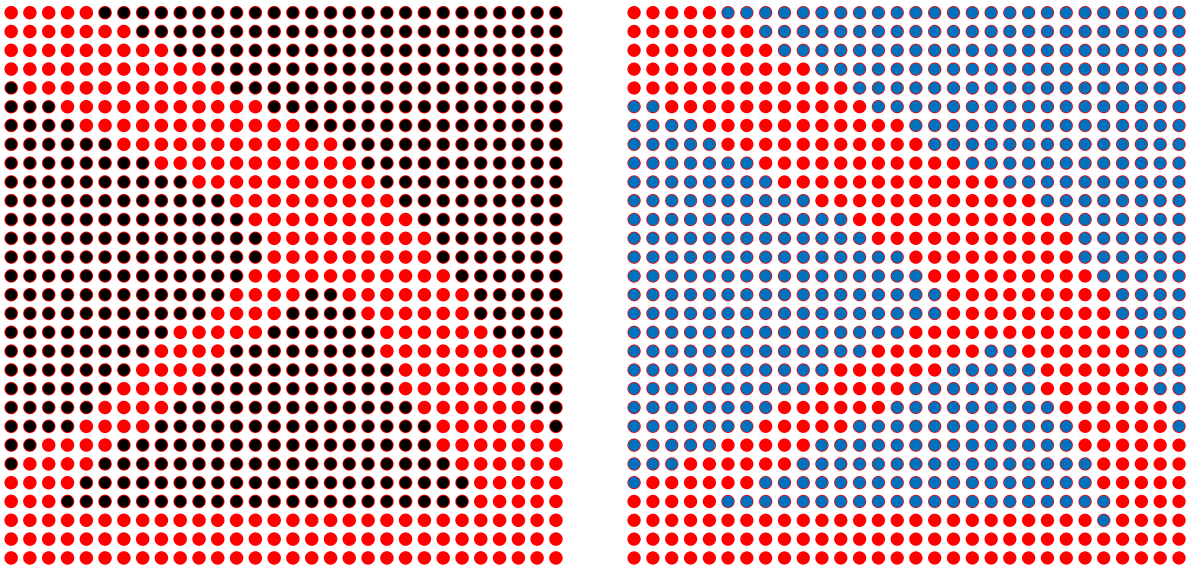

(a) RBFs-LSM (b) Conv-LSM

Figure 7: Comparison of EFG based RBFs-LSM and Conv-LSM [52]

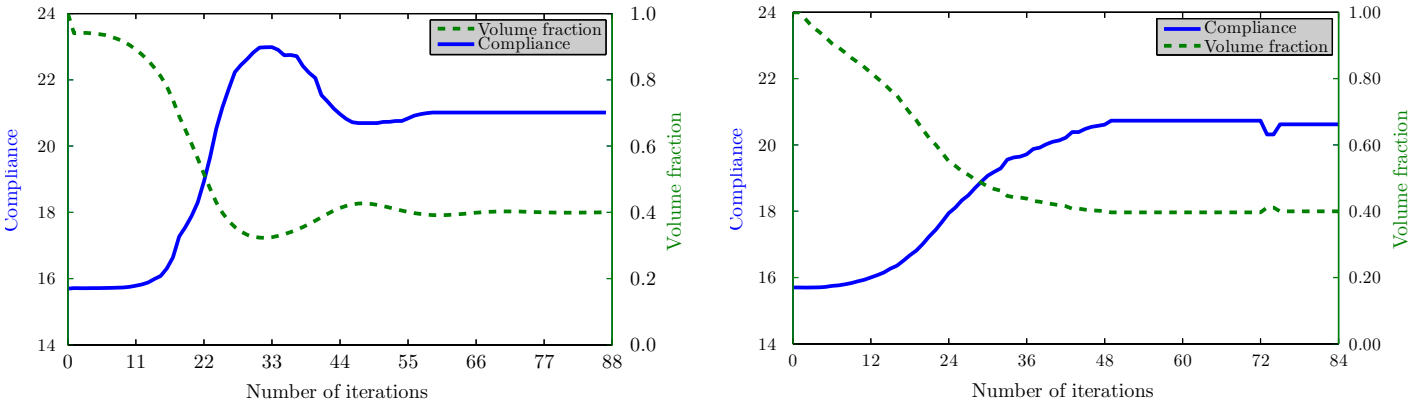

(a) RBFs-LSM (b) Conv-LSM [52]

Figure 8: Comparison of EFG based RBFs-LSM and Conv-LSM evolution of objective function and constraint

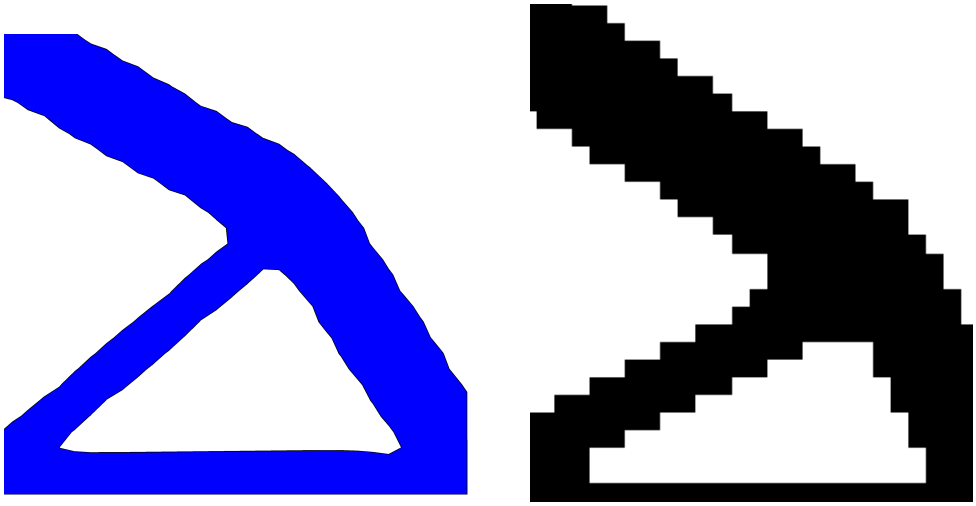

(a) RBFs-LSM (b) Conv-LSM

Figure 9: Comparison of EFG based RBFs-LSM and Conv-LSM [60]

6.2. Example-2

The second test problem is a cantilever beam with an aspect ratio of 1.6 : 1. The left side boundary is constrained in all directions and a unit load is applied at the centre of the right boundary. The initial geometry is illustrated in Fig. 10. The required volume fraction is taken as 50%. The problem domain is discretized with $61 \times 39 = 2379$ uniform nodes.

Figure 10: Design domain Example-2

Different stages of evolutionary process towards attaining optimal geometry are shown in Fig. 11, as meshless nodal points and in Fig. 12, as zero level set contours, respectively. The topological changes through hole creation and subsequent merging with each other and with the boundary is evident from the evolution history. The final optimal solution is obtained after 120 iterations, which is similar to optimal geometries reported in literature, e.g., [15, 31, 33, 63]. This further suggests that the proposed implementation effectively generates optimal designs with different geometry and loading conditions.

The optimal results are compared in Fig. 13 with the discrete level set method presented in [60]. The current method provides optimal results with better boundary description.

Fig. 14 shows the volume fraction and objective function curves during the optimization iterations.

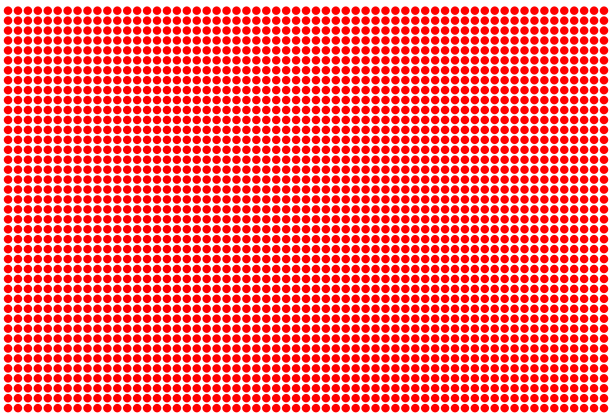

(a) Initial design

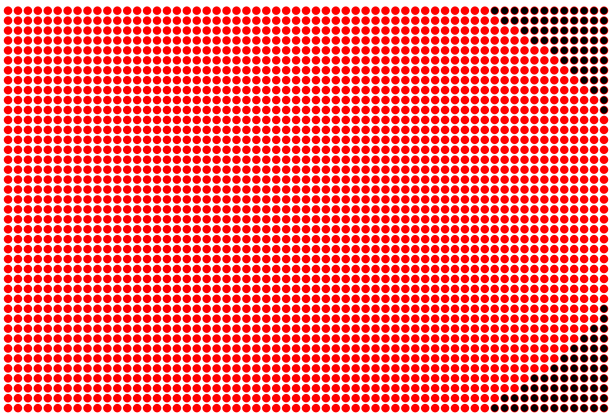

(b) Iteration 20

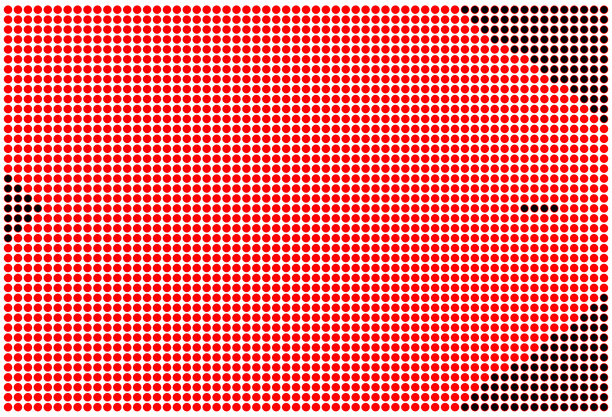

(c) Iteration 30

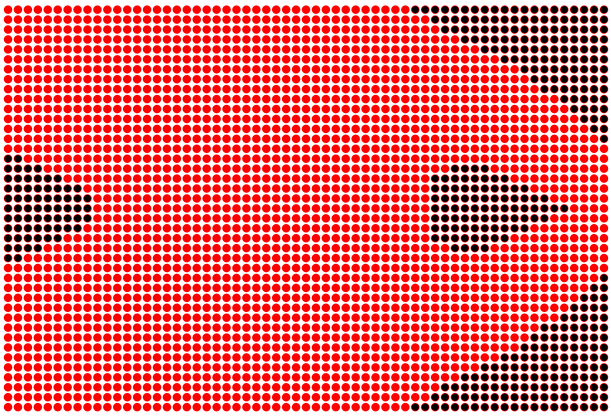

(d) Iteration 40

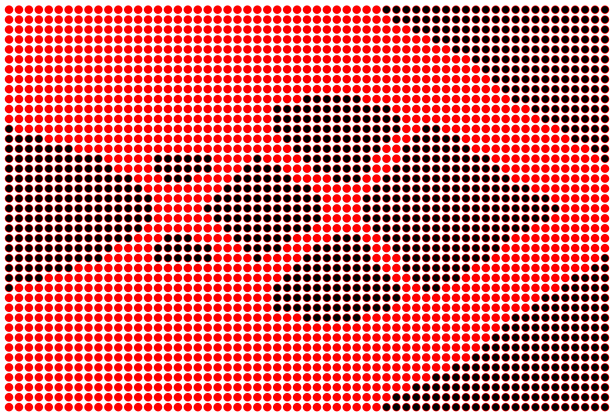

(e) Iteration 50

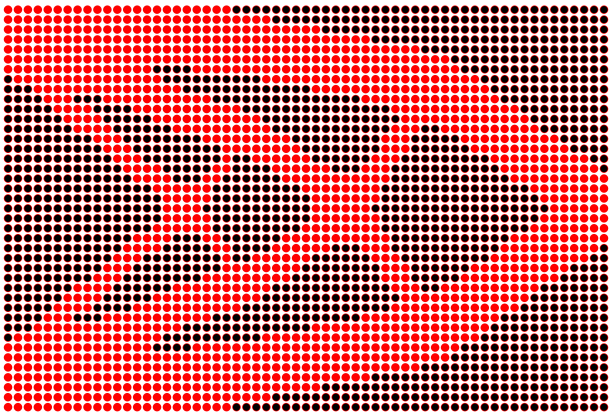

(f) Optimal design

Figure 11: Meshless nodal points plots for Example-2 with $V_{req} = 50\%$

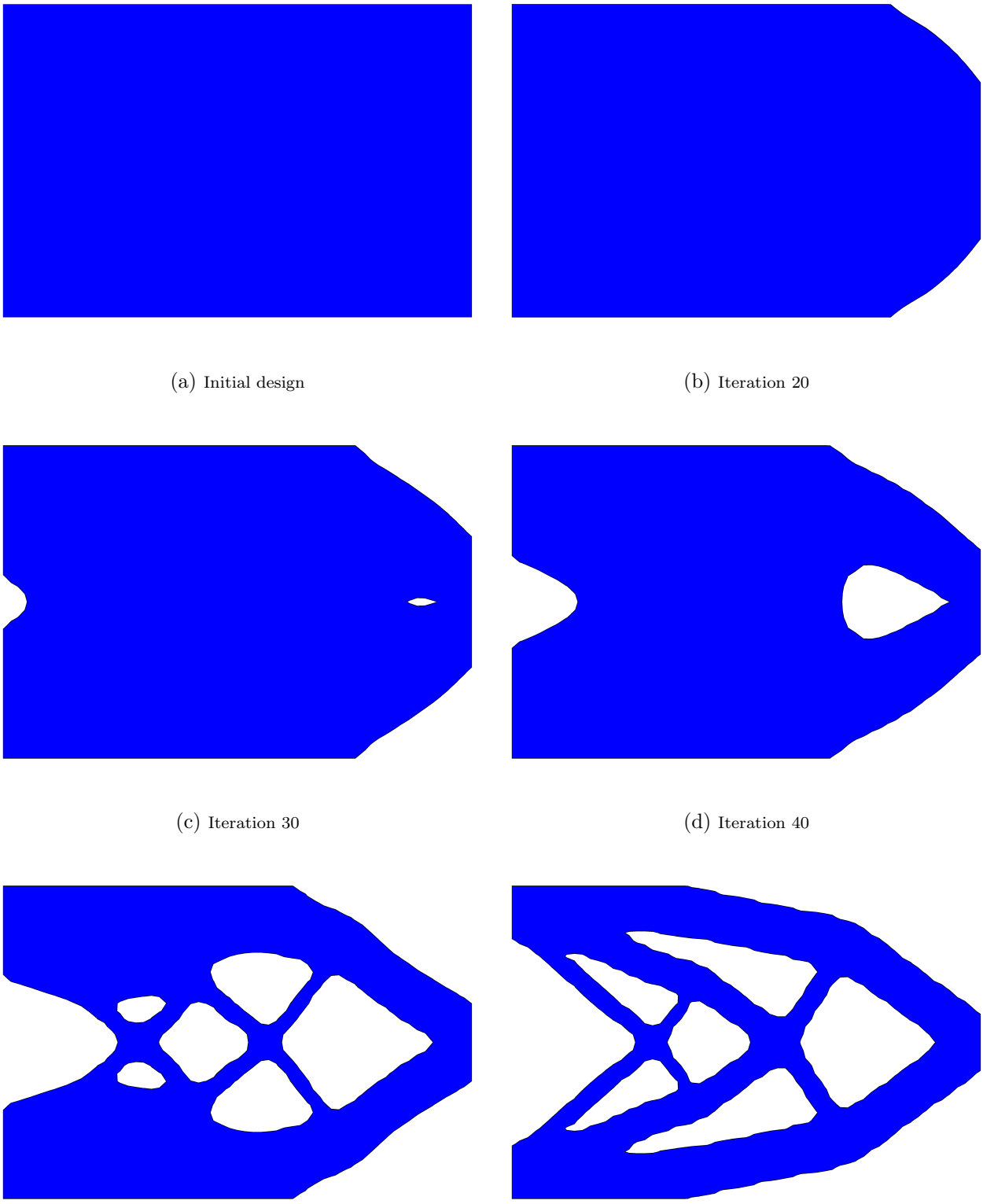

(a) Initial design

(b) Iteration 20

(c) Iteration 30

(d) Iteration 40

(e) Iteration 50

(f) Optimal design

Figure 12: Structural zero level set plots for Example-2 with $V_{req} = 50\%$

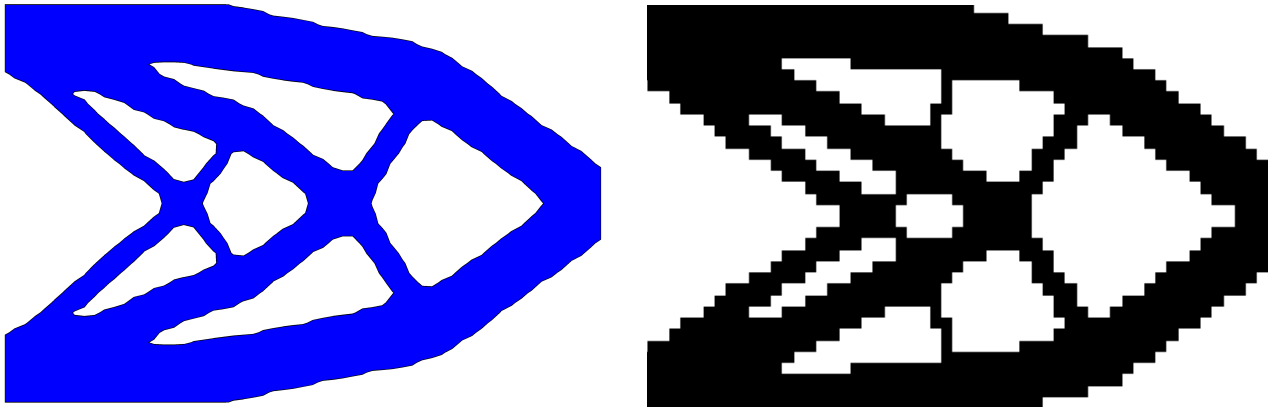

(a) RBFs-LSM (b) Conv-LSM

Figure 13: Comparison of EFG based RBFs-LSM and FEM based Conv-LSM [60]

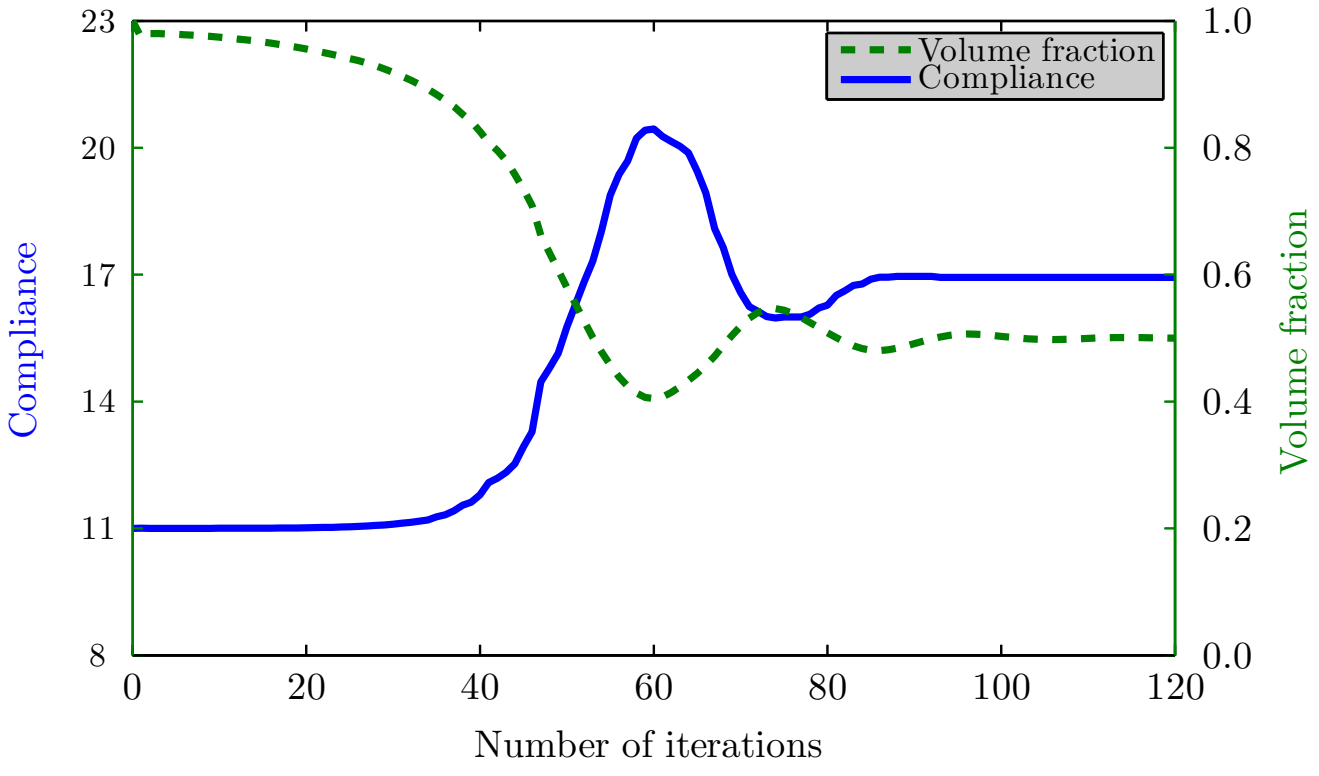

Figure 14: Objective function and volume constraint plot for Example-2 with $V_{req} = 50\%$

The same geometry is also solved for a different volume fraction, i.e., 30%, and the optimisation results are shown in Figs. 15 and 16, respectively. A direct comparison is also presented in Fig. 17 with SIMP method [64], which further suggests the validity of this new implementation.

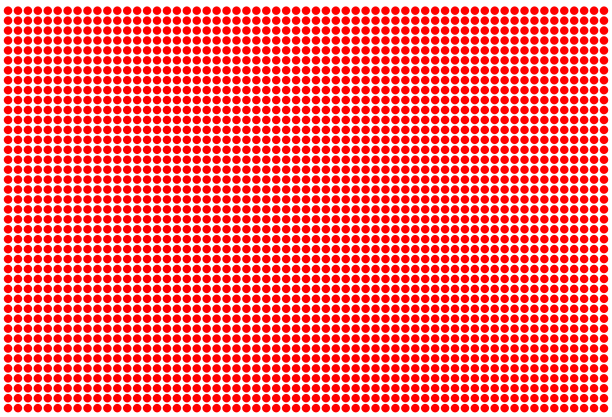

(a) Initial design

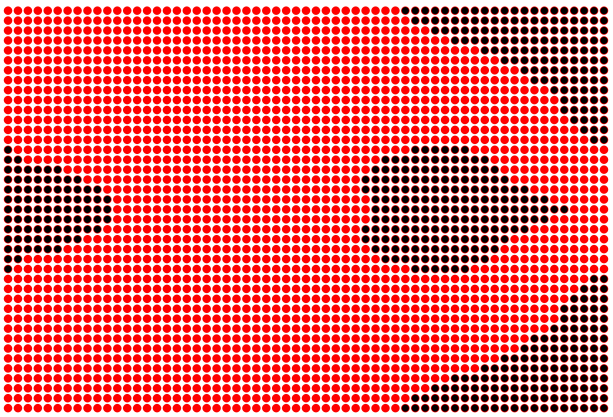

(b) Iteration 20

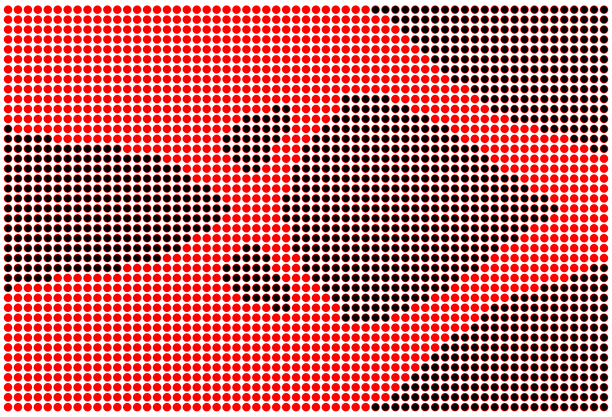

(c) Iteration 30

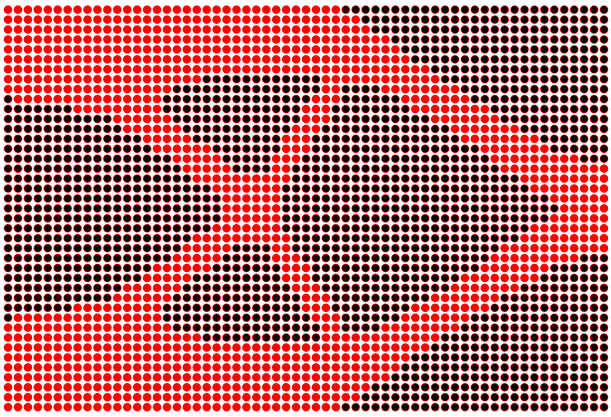

(d) Iteration 40

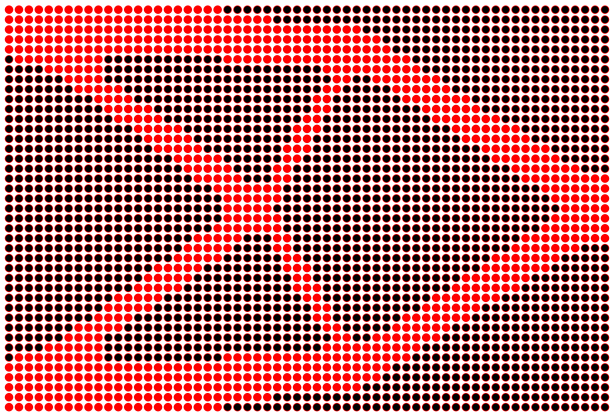

(e) Iteration 50

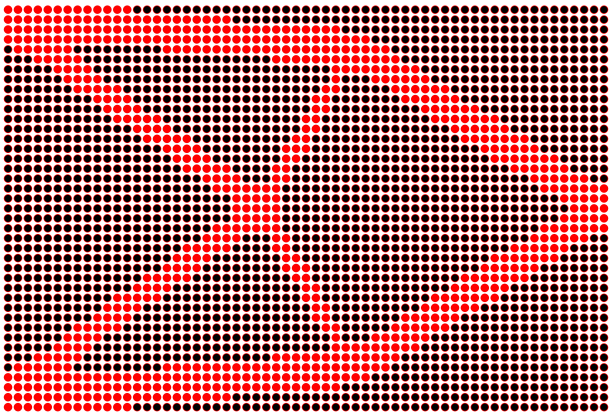

(f) Optimal design

Figure 15: Meshless nodal points plots for Example-2 with $V_{req} = 30\%$

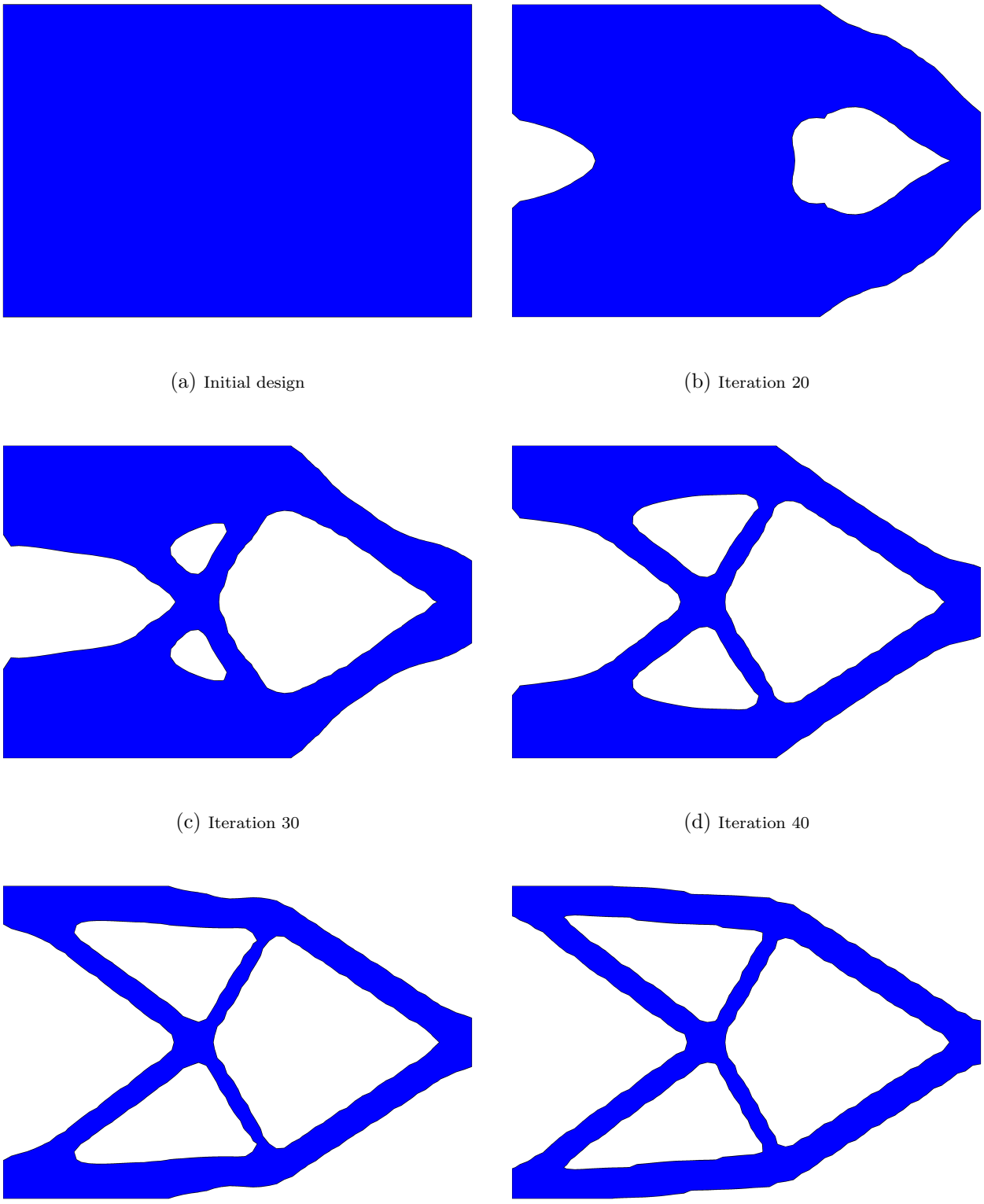

(a) Initial design

(b) Iteration 20

(c) Iteration 30

(d) Iteration 40

(e) Iteration 50

(f) Optimal design

Figure 16: Structural zero level set plots for Example-2 with $V_{req} = 30\%$

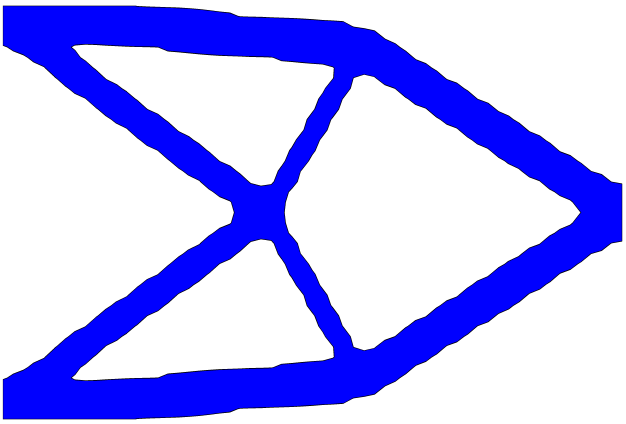

(a) RBFs-LSM

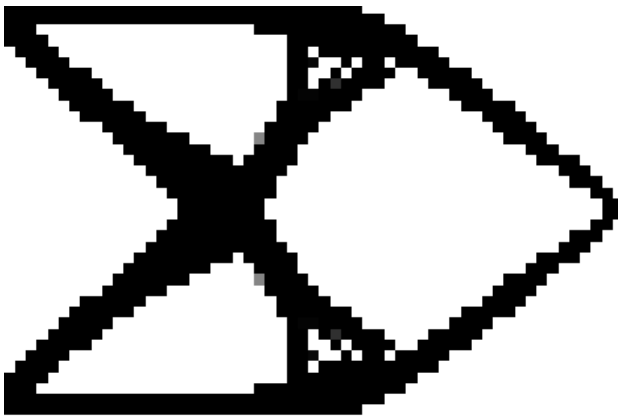

(b) SIMP without filter

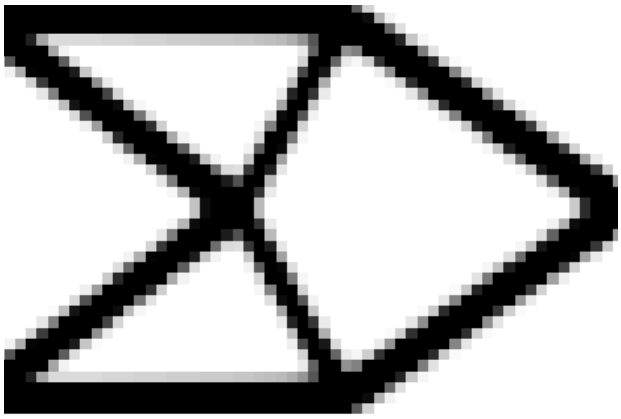

(c) SIMP without filter

Figure 17: Comparison of EFG based RBFs-LSM and SIMP [64]

6.3. Example-3

In this case a Michell type problem is considered with dimensions 2×1. The left and right hand portions of the bottom boundary are constrained in all directions and a unit load is applied at the centre in the downward direction. The structure initial configuration is illustrated in Fig. 18. The required volume fraction is taken as 50% of the initial design. A mesh size of $61 \times 31 = 1891$ is considered for the solution of this problem.

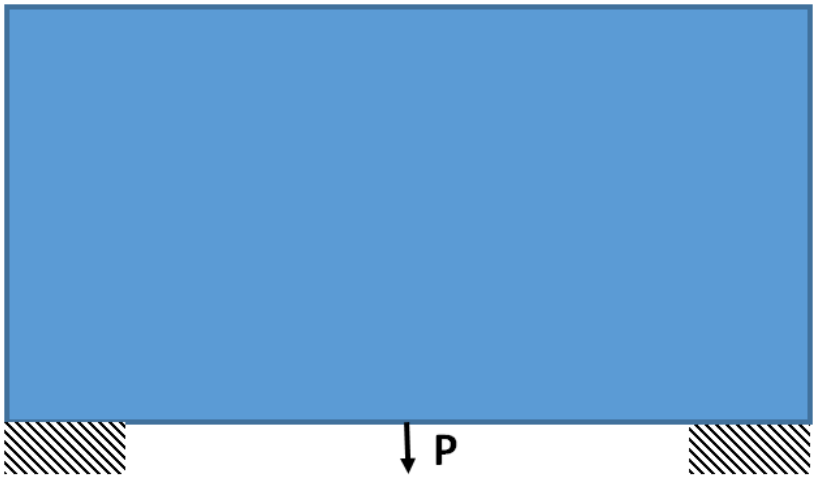

Figure 18: Design domain Example-3

The meshless nodal points plot and the evolving structural geometry is depicted in Figs. 19 and 20, respectively. The topological and shape changes are carried out with this unique combination of EFG and RBFs-LSM in a stable and efficient manner. The optimisation process converged after 93 iterations, once the stopping criterion is satisfied. The optimal geometry obtained through the proposed procedure is in close agreement with those reported in [15, 31, 33, 63]. It is evident from these results that the current implementation is capable to solve different benchmark problems effectively and efficiently

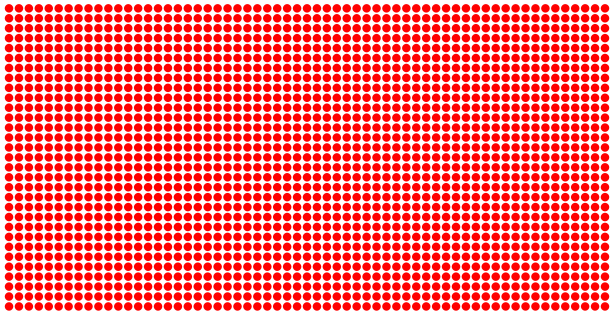

(a) Initial design

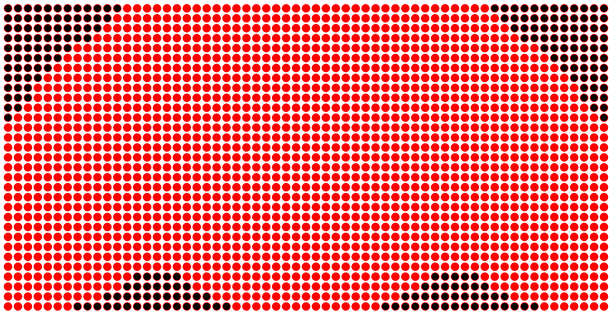

(b) Iteration 10

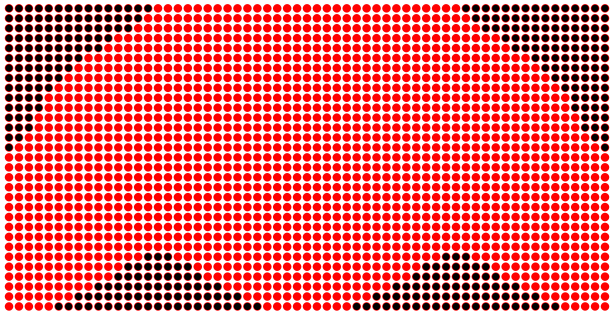

(c) Iteration 15

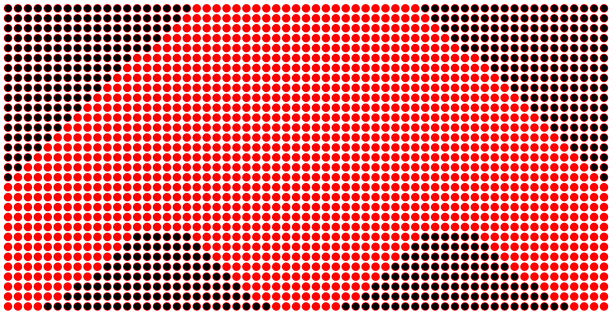

(d) Iteration 20

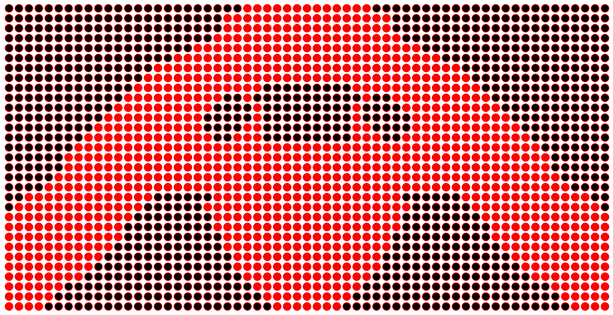

(e) Iteration 25

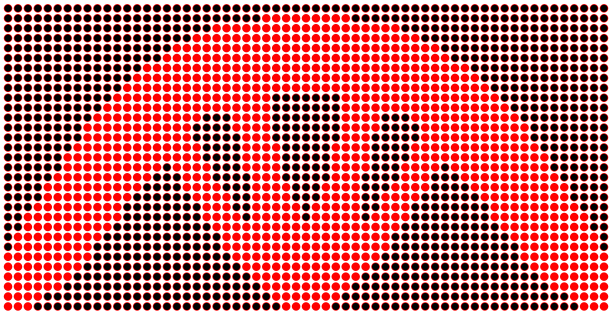

(f) Optimal design

Figure 19: Meshless nodal points plots for Example-3

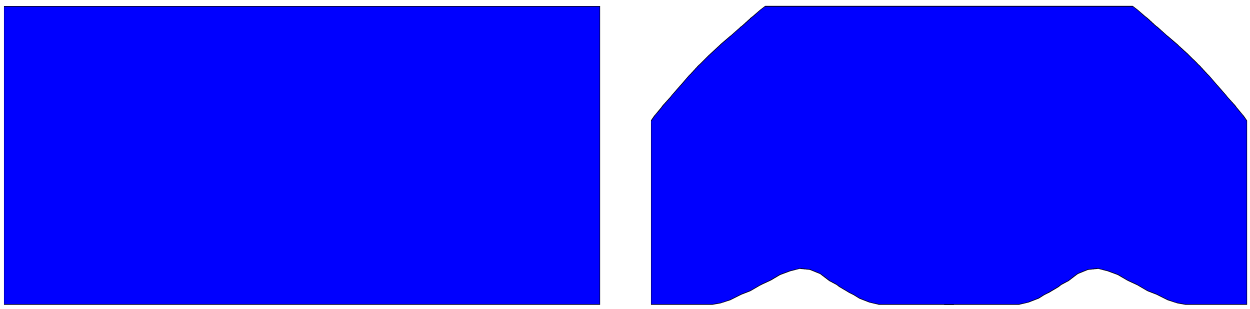

(a) Initial design

(b) Iteration 10

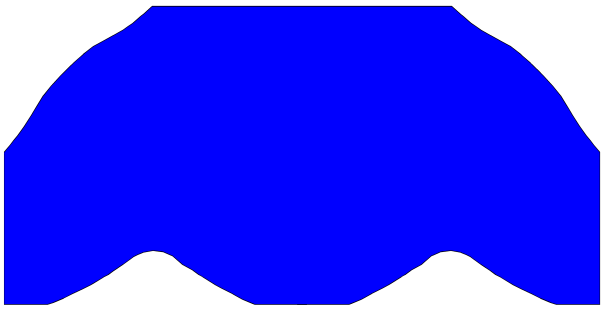

(c) Iteration 15

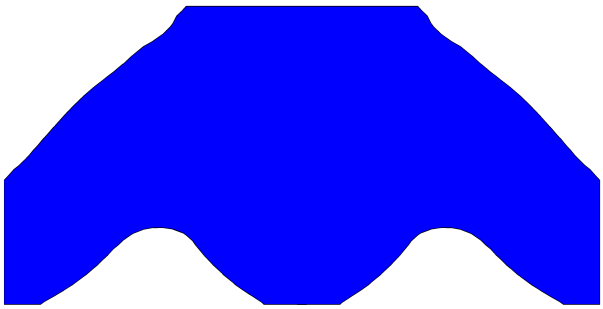

(d) Iteration 20

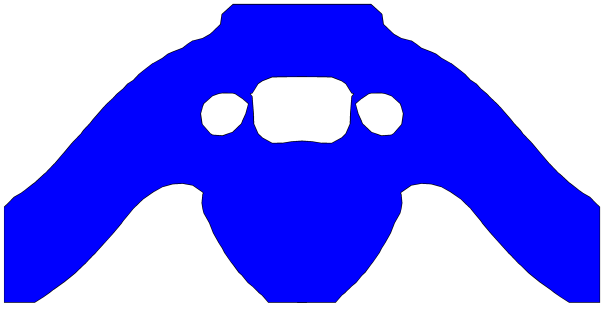

(e) Iteration 25

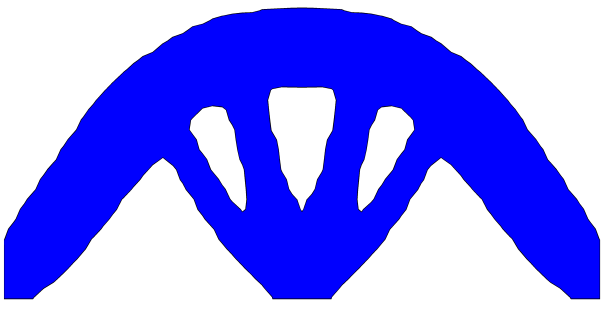

(f) Optimal design

Figure 20: Structural zero level set plots for Example-3

Fig. 21 shows the volume fraction and objective function curves versus the number of iterations. This clearly shows that the design objective is accomplished by improving the structural stiffness while the volume is preserved.

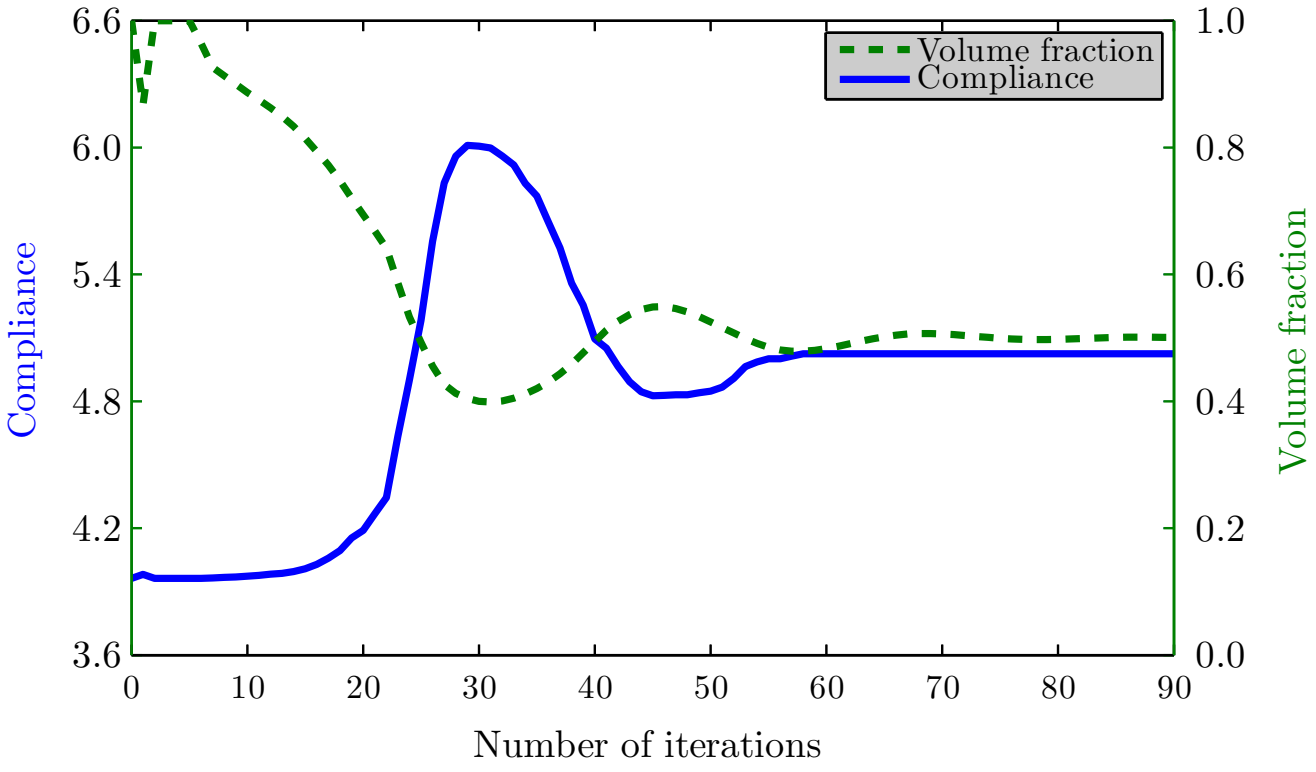

Figure 21: Objective function and volume constraint plot for Example-3

6.4. Example-4

The proposed approach is further tested with different geometry and boundary conditions using a cantilever beam with dimension 2×1 as depicted in Fig. 22. The left hand boundary is fixed and a unit load is applied at the bottom corner of the right hand boundary. The volume fraction V_{req} is set to 50%. The design domain is discretized with $61 \times 31 = 1891$ uniformly distributed nodes.

Figure 22: Design domain Example-4

The evolution of the optimal solution is shown in Figs. 23 and 24, respectively, where the process converged after 104 iterations. The optimal geometry obtained by the proposed procedure is in close resemblance with those reported in the literature [32, 64].

Fig. 25 shows the volume fraction and objective function evolution during the optimisation process. In the initial iterations, the compliance is gradually increasing as a result of the material removal, however, once the volume constraint is satisfied the same stabilizes in the subsequent iterations.

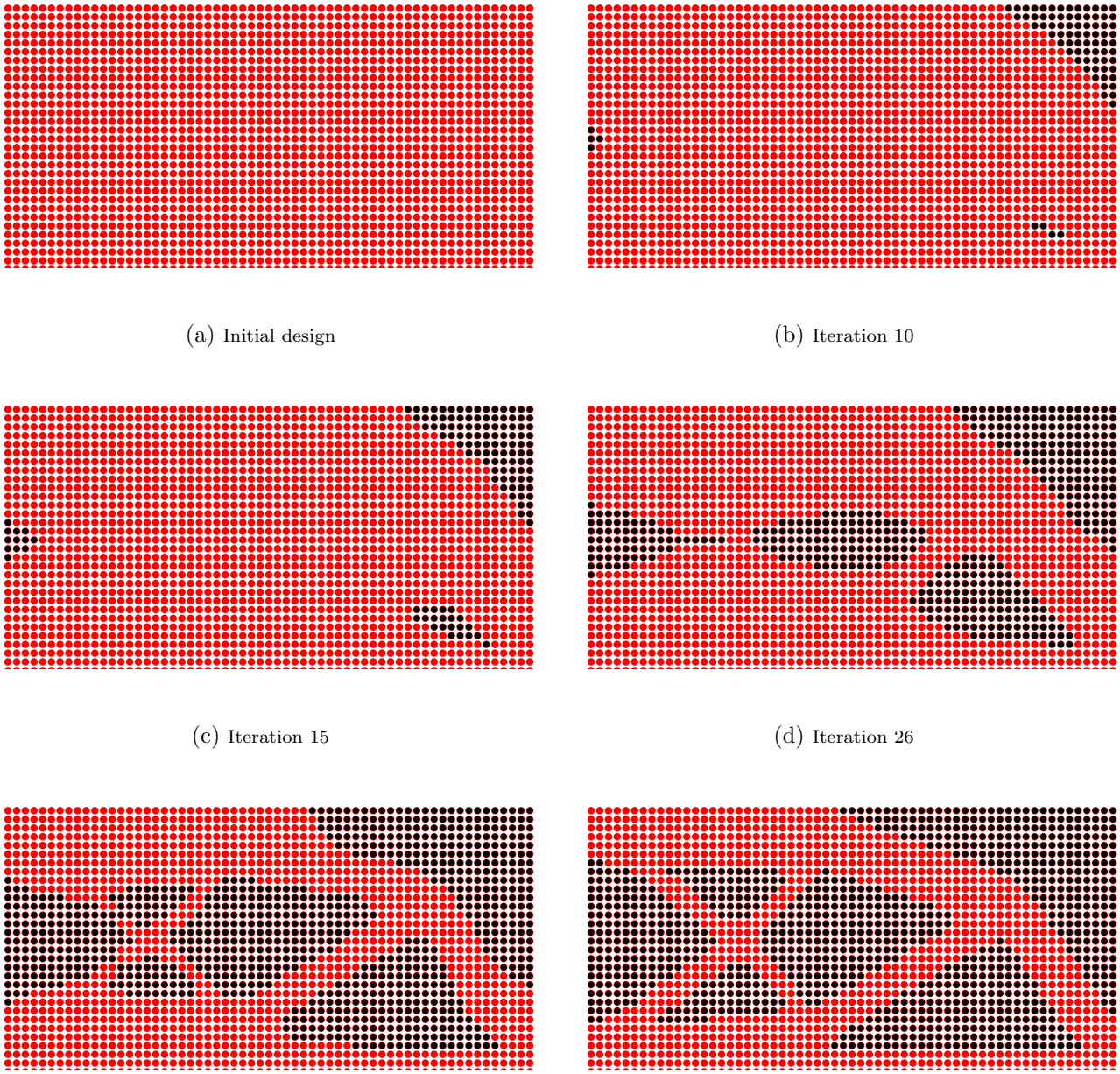

(a) Initial design

(b) Iteration 10

(c) Iteration 15

(d) Iteration 26

(e) Iteration 35

(f) Optimal design

Figure 23: Meshless nodal points plots for Example-4

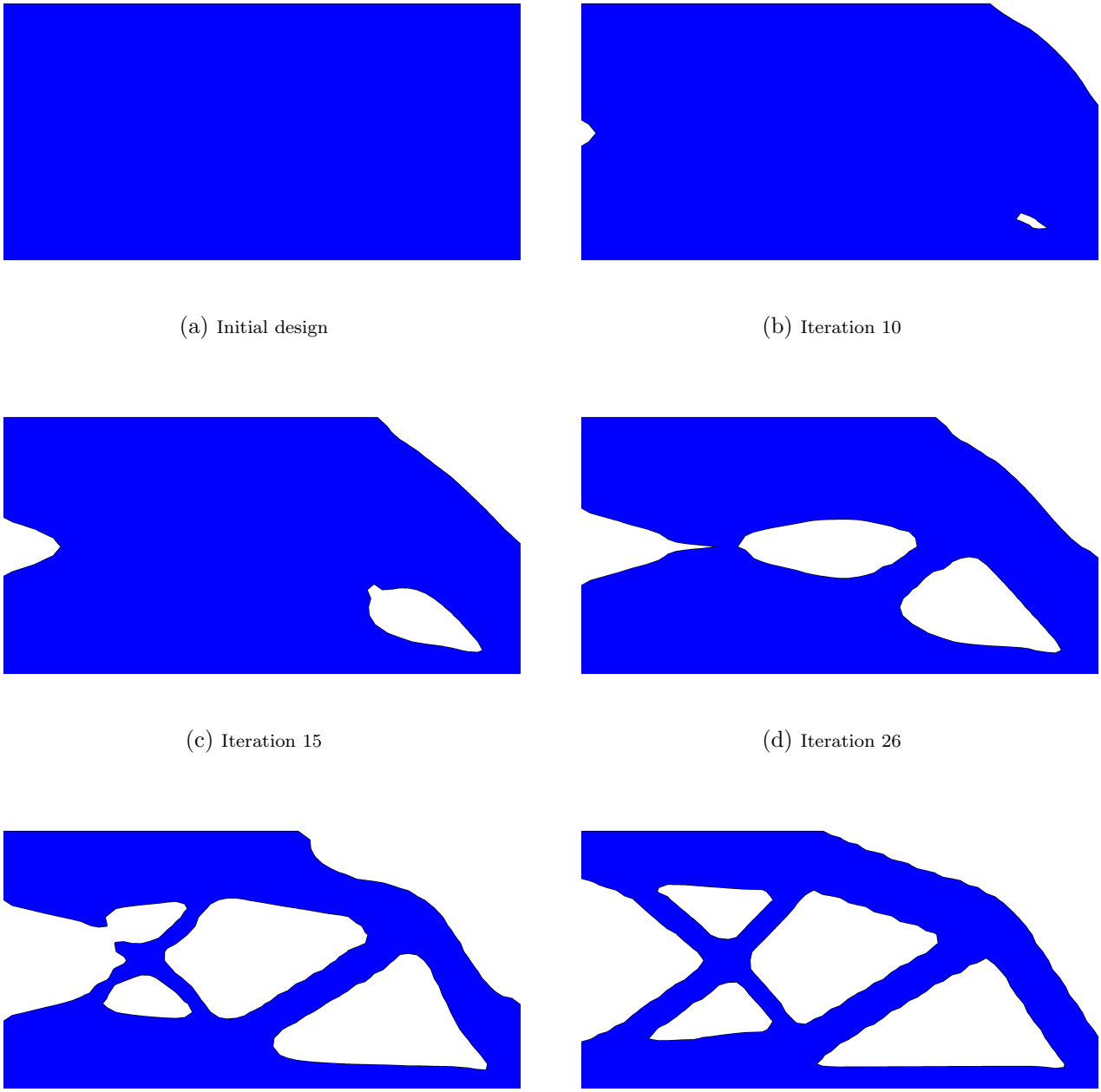

(a) Initial design

(b) Iteration 10

(c) Iteration 15

(d) Iteration 26

(e) Iteration 35

(f) Optimal design

Figure 24: Structural zero level set plots for Example-4

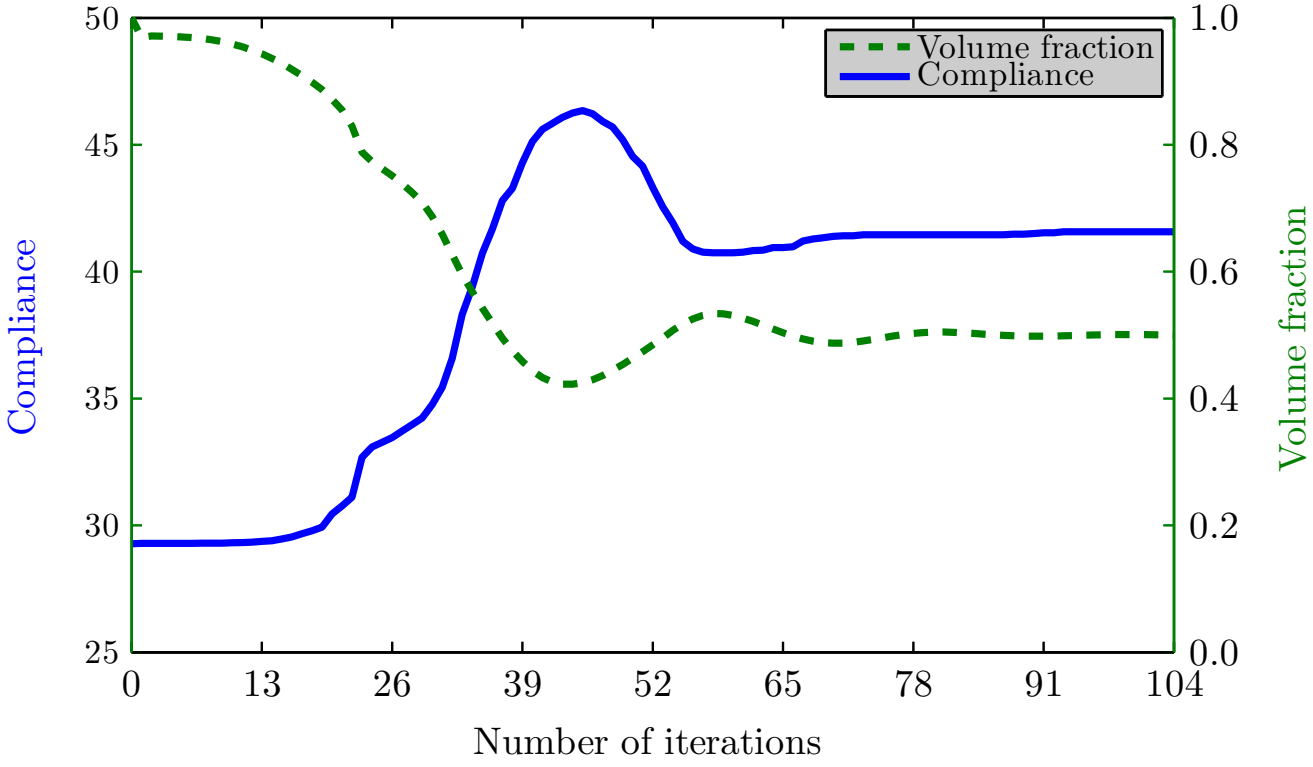

Figure 25: Objective function and volume constraint plot for Example-4

7. Conclusions

In this research work, the EFG method is integrated with RBFs based LSM for the solution of two dimensional topology optimization problems. An important aspect of this new implementation is the modelling of the moving boundary discontinuities without re-discretization. Moreover, the same computational grid is used for both the meshless EFG and RBFs-LSM, which simplified the optimization process and allowed significant saving of the overall computational efforts. During the optimization process, the proposed method has the capability of hole nucleation at appropriate locations within the design domain, thus eliminating the dependency of the initially guessed design. Different computational experiments are conducted to ascertain the accuracy, convergence and computational efficiency of the proposed optimization method. The optimal designs obtained from the proposed method show close resemblance with the same test cases reported in the literature.

In this research study the main reason of using EFG technique for the evaluation of structural response at each optimization step is summarized as follows:

- Conceptual simplicity of implementation, high accuracy and rapid convergence
- The use of a set of nodes rather than a mesh for numerical solution without any additional information of mesh connectivity, etc
- A single Cartesian grid for the evaluation of design sensitivities as well as the solution of level set equation for the evolution of structural geometry
- Straight forward extension to other mechanics problems with different physics, e.g., material as well as structural non-linearities, discontinuities and singularities, etc.

This will definitely open a new window for further exploration of the use of meshless methods for more advanced level optimization problems, to which other methods may not adequately provide reliable solutions. However, the proposed method is very sensitivity with respect to some optimization parameters as compared to the method in [52]. Also the computational cost of the meshless methods is on higher side than the mesh based methods due to the non-banded structure of the coefficient matrix.

Acknowledgements

The data that support the findings of this study are available from the author's, upon reasonable request. Finally, the author's confirm that there are no relevant financial or non-financial competing interests to report.

References

[1] D. Wang, W. Zhang, J. Jiang, Combined shape and sizing optimization of truss structures, Computational Mechanics 29 (4-5) (2002) 307–312.

[2] Li. Xiaolin and Li. Shuling, A fast element-free Galerkin method for the fractional diffusion-wave equation, Applied Mathematics Letters, 122,107–529,2021,

[3] Li, Xiaolin and Li, Shuling, A linearized element-free Galerkin method for the complex Ginzburg–Landau equation, Computers & Mathematics with Applications,90,135–147,2021

[4] J. Sokołowski, J. Zolesio, Introduction to Shape Optimization: Shape Sensitivity Analysis. 1992, Springer, Heidelberg.

[5] M. Bendsoe, Sigmund, Topology Optimization-Theory, Methods and Applications, Springer, 2003.

[6] L. Dedè, M. J. Borden, T. J. Hughes, Isogeometric analysis for topology optimization with a phase field model, Archives of Computational Methods in Engineering 19 (3) (2012) 427–465.

[7] Q. X. Lieu, J. Lee, A multi-resolution approach for multi-material topology optimization based on isogeometric analysis, Computer Methods in Applied Mechanics and Engineering 323 (2017) 272–302.

[8] M. P. Bendsøe, N. Kikuchi, Generating optimal topologies in structural design using a homogenization method, Computer Methods in Applied Mechanics and Engineering 71 (2) (1988) 197–224.

[9] K. Suzuki, N. Kikuchi, A homogenization method for shape and topology optimization, Computer Methods in Applied Mechanics and Engineering 93 (3) (1991) 291–318.

[10] G. Allaire, R. V. Kohn, Optimal design for minimum weight and compliance in plane stress using extremal microstructures, European Journal of Mechanics. A. Solids 12 (6) (1993) 839–878.

[11] M. P. Bendsøe, O. Sigmund, Material interpolation schemes in topology optimization, Archive of Applied Mechanics 69 (9-10) (1999) 635–654.

[12] Y. M. Xie, G. P. Steven, A simple evolutionary procedure for structural optimization, Computers & Structures 49 (5) (1993) 885–896.

[13] G. O. Querin, Y. Xie, Evolutionary structural optimisation (ESO) using a bidirectional algorithm, Engineering Computations 15 (1998) 1031–1048,.

[14] W. Wang, Michael Yu, Guo, Dongming, A level set method for structural topology optimization, Computer Methods in Applied Mechanics and Engineering 192 (1) (2003) 227–246.

[15] G. Allaire, F. Jouve, A.-M. Toader, Structural optimization using sensitivity analysis and a level-set method, Journal of Computational Physics 194 (1) (2004) 363–393.

[16] H. L. Oliveira, H. de Castroe Andrade, E. D. Leonel, An isogeometric boundary element approach for topology optimization using the level set method, Applied Mathematical Modelling 84 (2020) 536 – 553.

[17] G. Jing, H. Isakari, T. Matsumoto, T. Yamada, T. Takahashi, Level set-based topology optimization for 2D heat conduction problems using BEM with objective function defined on design-dependent boundary with heat transfer boundary condition, Engineering Analysis with Boundary Elements 61 (2015) 61–70.

[18] M. P. Bendsoe, O. Sigmund, Topology optimization: theory, methods, and applications, Springer Science & Business Media, 2013.

[19] Z. Luo, N. Zhang, Y. Wang, W. Gao, Topology optimization of structures using meshless density variable approximants, International Journal for Numerical Methods in Engineering 93 (4) (2013) 443–464.

[20] X. Huang, Y. M. Xie, Convergent and mesh-independent solutions for the bi-directional evolutionary structural optimization method, Finite Elements in Analysis and Design 43 (14) (2007) 1039 – 1049.

[21] S. Osher, J. A. Sethian, Fronts propagating with curvature-dependent speed: algorithms based on hamilton-jacobi formulations, Journal of Computational Physics 79 (1) (1988) 12–49.

[22] S. Osher, R. P. Fedkiw, Level set methods: an overview and some recent results, Journal of Computational Physics 169 (2) (2001) 463–502.

[23] J. A. Sethian, A. Wiegmann, Structural boundary design via level set and immersed interface methods, Journal of Computational Physics 163 (2) (2000) 489–528.

[24] J. A. Sethian, Level set methods and fast marching methods: evolving interfaces in computational geometry, fluid mechanics, computer vision and materials science., Vol. 3, Cambridge Monographs on Applied and Computational Mathematics, Cambridge University Press, Cambridge, 1999.

[25] J. C. Ye, Y. Bresler, P. Moulin, A self-referencing level-set method for image reconstruction from sparse fourier samples, International Journal of Computer Vision 50 (3) (2002) 253–270.

[26] Osher S, Fedkiw RP, Level set methods: an overview and some recent results, Journal of Computational Physics 169 (2) (2001) 463–502.

[27] F. Osher S, Level set methods and dynamic implicit surfaces, Springer, New York.

[28] H. Ghasemi, H. S. Park, T. Rabczuk, A multi-material level set-based topology optimization of flexoelectric composites, Computer Methods in Applied Mechanics and Engineering 332 (2018) 47–62.

[29] G. Allaire, F. De Gournay, F. Jouve, A.-M. Toader, Structural optimization using topological and shape sensitivity via a level set method, Control and Cybernetics 34 (1) (2005) 59.

[30] T. Yamada, K. Izui, S. Nishiwaki, A. Takezawa, A topology optimization method based on the level set method incorporating a fictitious interface energy, Computer Methods in Applied Mechanics and Engineering 199 (45-48) (2010) 2876–2891.

[31] S. Wang, K. Lim, B. C. Khoo, M. Y. Wang, An extended level set method for shape and topology optimization, Journal of Computational Physics 221 (1) (2007) 395–421.

[32] J. Luo, Z. Luo, L. Chen, L. Tong, M. Y. Wang, A semi-implicit level set method for structural shape and topology optimization, Journal of Computational Physics 227 (11) (2008) 5561–5581.

[33] B. Ullah, J. Trevelyan, A boundary element and level set based topology optimisation using sensitivity analysis, Engineering Analysis with Boundary Elements 70 (2016) 80–98.

[34] S. Wang, M. Y. Wang, Radial basis functions and level set method for structural topology optimization, International Journal for Numerical Methods in Engineering 65 (12) (2006) 2060–2090.

[35] T. Cecil, J. Qian, S. Osher, Numerical methods for higher dimensional HamiltonJacobi equations using radial basis functions, Journal of Computational Physics 196 (2004) 327–347.

[36] Z. Luo, L. Tong, Z. Kang, A level set method for structural shape and topology optimization using radial basis functions, Computers & Structures 87 (7-8) (2009) 425–434.

[37] M. Otomori, T. Yamada, K. Izui, S. Nishiwaki, Matlab code for a level set-based topology optimization method using a reaction diffusion equation, Structural and Multidisciplinary Optimization 51 (5) (2015) 1159–1172.

[38] P. Wei, Z. Li, X. Li, M. Y. Wang, An 88-line matlab code for the parameterized level set method based topology optimization using radial basis functions, Structural and Multidisciplinary Optimization (2018) 1–19.

[39] X. Xie, M. Mirmehdi, Radial basis function based level set interpolation and evolution for deformable modelling, Image and Vision Computing 29 (2-3) (2011) 167–177.

[40] Y. Liu, Z. Li, P. Wei, W. Wang, Parameterized level-set topology optimization method considering symmetry and pattern repetition constraints, Computer Methods in Applied Mechanics and Engineering 340 (2018) 1079–1101.

[41] L. Shuling, L. Xiaolin, Radial basis functions and level set method for image segmentation using partial differential equation, Applied Mathematics and Computation 286 (2016) 29–40.

[42] G. R. Liu, Meshfree Methods Moving Beyond the Finite Element Method, CRC Press, 2003.

[43] G. R. Liu, Y. T. Gu, An introduction to Meshfree Methods and their Programming, Springer Netherlands, 2005.

[44] G. F. Fasshauer, Meshfree Apprixmation Methods with MATLAB, World Scientific Press Singapore, 2008.

[45] A. Krowiak, Domain-type rbf collocation methods for biharmonic problems, International Journal of Computational Methods 15 (08) (2018) 1850078.

[46] J. J. Monaghan, R.A.Gingold, Smoothed particle hydrodynamics: theory and application to non-spherical stars, Monthly Notices of the Royal Astronomical Society 181 (1977) 375–389.

[47] Y. T. Belytschko, L. Gu, Element-free galerkin methods, International Journal for Numerical Methods in Engineering 37 (1994) 229–256.

[48] X. Liu, G. R. Liu, K. Tai, K. Y. Lam, Radial point interpolation collocation method RPICM for the solution of nonlinear Poisson's problems, Computational Mechanics 36 (4) (2005) 298–306.

[49] W. K. Liu, S. Jun, Y. F. Zhang, Reproducing kernel particle methods, International Journal for Numerical Methods in Fluids 20 (8-9) (1995) 1081–1106.

[50] I. Bubuska, J. Melenk, The partition of unity method, International Journal of Numerical Methods in Engineering 40 (1997) 727–728.

[51] S. N. Atluri, H. G. Kim, J. Y. Cho, A critical assessment of the truly Meshless Local Petrov Galerkin (MLPG), and Local Boundary Integral Equation (LBIE) methods, Computational Mechanics 24 (1999) 348–372.

[52] W. Khan, Siraj-ul-Islam, B. Ullah, Structural optimization based on meshless element free Galerkin and level set methods, Computer Methods in Applied Mechanics and Engineering 344 (2019) 144–163.

[53] T. Belytschko, Y. Krongauz, D. Organ, M. Fleming, P. Krysl, Meshless methods: an overview and recent developments, Computer Methods in Applied Mechanics and Engineering 139 (1-4) (1996) 3–47.

[54] G. R. Liu, Y. T. Gu, An introduction to meshfree method and their programming, Published by Springer, 2005.

[55] Lancaster, P. Salkauskas, Surfaces generated by moving least squares methods, Math. Comput. 37 (1981) 141–158.

[56] B. Nayroles, G. Touzot, P. Villon, Generalizing the finite element method: diffuse approximation and diffuse elements, Computational Mechanics 10 (5) (1992) 307–318.

[57] Y.Y. Lu, T. Belytschko, L. Gu, A new implementation of the element free Galerkin method, Computational Methods and Applied Mechanical Engineering 113 (1994) 397–414.

[58] R. Tsai, S. Osher, Level set methods and their applications in image science, Communications in Mathematical Sciences 4 (1) (2003) 623–656.

[59] E. Kansa, H. Power, G. Fasshauer, L. Ling, A volumetric integral radial basis function method for time-dependent partial differential equations. I. formulation, Engineering Analysis with Boundary Elements 28 (10) (2004) 1191–1206.

[60] V. Challis, A discrete level-set topology optimization code written in matlab, Struct Multidisc Optim 41 (2010) 453–464.

[61] B. Ullah, J. Trevelyan, Correlation between hole insertion criteria in a boundary element and level set based topology optimisation method, Engineering Analysis with Boundary Elements 37 (11) (2013) 1457–1470.

[62] R. J. Marczak, Optimization of elastic structures using boundary elements and a topological-shape sensitivity formulation, Latin American Journal of Solids and Structures 5 (2008) 99–117.

[63] H. A. Jahangiry, S. M. Tavakkoli, An isogeometrical approach to structural level set topology optimization, Computer Methods in Applied Mechanics and Engineering 319 (2017) 240–257.

[64] O. Sigmund, A 99 line topology optimization code written in matlab, Structural and Multidisciplinary Optimization 21 (2) (2001) 120–127.